Multiparameter inverse scattering: preliminary testing results

Glen R. Young, Kris Innanen and Laurence R. Lines

ABSTRACT

The use of inverse scattering methods in the inversion of seismic data has been on the rise in exploration geophysics. With specific computational approaches it is possible to ascertain the material properties of the subsurface using scattered acoustic waves. We seek to determine multiple rock parameters such as density and bulk modulus from reflected seismic signals. A basic approach is used based on straightforward inverse scattering equations. In this case we will examine how multiparameter inverse scattering in a constant 2D background works and what are the results of inverting synthetically generated data.

A simulation was developed for this project in two parts. The forward modeling/migration stage is covered in Young et al (2011) and the least squares inversion of the data for rock properties is covered in this report. The inversion imagery is examined for accuracy and various models are tested to determine if physically realistic effects are present as would be seen in real seismic data. The conclusion from doing linearized Born inversion is that it is successful in mapping out the 'perturbing' subsurface structure, the results for a two parameter approach seem realistic, a knowledge of the background velocity and also the constant background density would allow for the determination of the absolute values of the rock properties of interfaces at depth.

INTRODUCTION

In the field of exploration geophysics, the inversion of seismic data obtained from expensive seismic survey operations is of paramount importance to various resource based industries. Specifically in the interpretation and location of petroleum bearing subsurface formations as well as in general subsurface mapping of other geologic structures for economic and scientific purposes.

The knowledge of the physical parameters of subsurface structures is vitally important in the exploration process, these telltale indicators are the guide to which many other decisions in the economic exploitation chain are made. The proper interpretation of these indicators yields successful recovery operations, the failure to gain accurate data for these interpretations can lead to unwanted and wasteful expenditures of time and money.

We detail here one of the algorithms published in Clayton and Stolt (1981). The two parts to the simulation chain are the forward modelling and the inversion. In the forward model we will use standard routines found within the CREWES Matlab toolkit and is used to generate the synthetic seismic data in the form of 2D shot profile and various velocity models. The inversion portion and management of its computational issues is our new contribution and is found in this paper.

This is the second half of the report started in, Young et al (2011), in it we will investigate the results of inversion performed on forward modeled data derived from the three models presented previously and add another case for investigation. The Clayton and Stolt

algorithm derived in their paper is for a two parameter inversion which is investigated here. Three variants of the one parameter case are investigated here, a simple 1-D inversion, a 1.5D case where the model is uniform along the x(offset) axis, and a 2D version where the model is not uniform about the x axis. An examination of the accuracy and quality of the results will be done on a case by case basis.

Mostly qualitative conclusions about the accuracy and quality of each model are illustrated with plots of the results and the supporting information for each case. For the purposes of accuracy the input velocity models were all regridded to a 5m spacing instead of a 10m spacing, this eliminated or severely reduced some artifacts such as grid dispersion and undersampling which could affect the accuracy of the results and can cause other issues with the fidelity of the results.

Inversion Methodology

Born inversion is a high frequency method in the Fourier (frequency) domain and is computationally more efficient and faster because a time-space domain convolution operation is simply a matrix multiplication in the wavenumber-frequency domain. The basic mathematical theory and method was outlined in Young et al (2011) and the mathematical foundation is included in Appendix B, in this section we describe the implementation of the algorithms to compute the migration and inversion images.

Least Squares Method of Clayton and Stolt

In the paper by Clayton and Stolt (1981) and from eqn. 51 we can expand the expression further to determine a least squares formula for the one and two parameter cases. Starting with the result for the deconvolved data $D'(k_m, k_z, k_h)$

$$D'(k_m, k_z, k_h) = \left[\sum_{i=1}^{2} A_i(k_m, k_h, k_z) a_i(k_m, k_z) \right], \tag{1}$$

which is a statement of the inverse problem. The a_i are independent of k_h so that any two distinct k_h values will output values of a_1 and a_2. In a standard seimic survey there are usually many values of k_h which means our problem is overdetermined.

Clayton and Stolt (1981) recommends using a least squares approach for the solution of this problem. The general set of equations in matrix form is usually given by

$$\begin{bmatrix} \Sigma A_1^2 & \Sigma A_1 A_2 \\ \Sigma A_1 A_2 D' & \Sigma A_2^2 \end{bmatrix} \begin{bmatrix} a_1(k_m, k_z) \\ a_2(k_m, k_z) \end{bmatrix} = \begin{bmatrix} \Sigma A_1 D' \\ \Sigma A_2 D' \end{bmatrix} \tag{2}$$

where the summation is taken over k_h values. So we simply need the matrix inverse of this given by

$$\begin{bmatrix} a_1(k_m, k_z) \\ a_2(k_m, k_z) \end{bmatrix} = \begin{bmatrix} \Sigma A_1 D' \\ \Sigma A_2 D' \end{bmatrix} \begin{bmatrix} \Sigma A_1^2 & \Sigma A_1 A_2 \\ \Sigma A_1 A_2 D' & \Sigma A_2^2 \end{bmatrix}^{-1} \tag{3}$$

Using Kramer's Rule we can formally write

$$a_1(k_m, k_z) = \frac{\begin{vmatrix} \Sigma A_1(k_m, k_z, k_h) D'(k_m, k_z) & \Sigma A_1(k_m, k_z, k_h) A_2(k_m, k_z, k_h) \\ \Sigma A_2(k_m, k_z, k_h) D'(k_m, k_z) & \Sigma A_2^2(k_m, k_z, k_h) \end{vmatrix}}{\begin{vmatrix} \Sigma A_1^2(k_m, k_z, k_h) & \Sigma A_1(k_m, k_z, k_h) A_2(k_m, k_z, k_h) \\ \Sigma A_1(k_m, k_z, k_h) A_2(k_m, k_z, k_h) & \Sigma A_2^2(k_m, k_z, k_h) \end{vmatrix}} \tag{4}$$

$$a_2(k_m, k_z) = \frac{\begin{vmatrix} \Sigma A_1^2(k_m, k_z, k_h) & \Sigma A_1(k_m, k_z, k_h) D'(k_m, k_z) \\ \Sigma A_1(k_m, k_z, k_h) A_2(k_m, k_z, k_h) & \Sigma A_2(k_m, k_z, k_h) D'(k_m, k_z) \end{vmatrix}}{\begin{vmatrix} \Sigma A_1^2(k_m, k_z, k_h) & \Sigma A_1(k_m, k_z, k_h) A_2(k_m, k_z, k_h) \\ \Sigma A_1(k_m, k_z, k_h) A_2(k_m, k_z, k_h) & \Sigma A_2^2(k_m, k_z, k_h) \end{vmatrix}} \tag{5}$$

this is for a two parameter solution.

Of course other types of objective functions can be used but we are following the recommendations in this paper.

One thing needs to be mentioned, a constraining expression in this least squares procedure given in Clayton and Stolt (1981), is shown as $|k_h k_m| < |k_z|^2$, this formula states that the evanescent zone in k-space is to be excluded from the calculation of the parameters, $a_1(k_m, k_z)$ and $a_2(k_m, k_z)$ because of the limitations of the Born approximation. This is for the two parameter case where k_h is not zero. The limitation of usable values in k-space will affect the quality of the final spatial domain image, with less k-values meaning a loss of resolution in the (x,z) image space. As we will see the larger the number of k_h values used the more we can distinguish between the a_1 and a_2 parameters.

Fourier transform back to (x,z) space.

Once we have the parameters $a_1(k_m, k_z)$ and $a_2(k_m, k_z)$ we note these values are in Fourier space and like D' can be 2D Fourier transformed back into (x,z) space.

$$D(x, z) = \mathscr{F}\{D'(k_m, k_z)\}, \tag{6}$$

$$\tilde{a}_1(x, z) = \mathscr{F}\{a_1(k_m, k_z)\}, \tag{7}$$

$$\tilde{a}_2(x, z) = \mathscr{F}\{a_2(k_m, k_z)\}, \tag{8}$$

where $\tilde{a}_1(x, z)$ and $\tilde{a}_2(x, z)$ designate the Fourier transformed material parameters.

Migration Image

Computing $D(x, z)$ will give us the migrated image of the seismic data, however $\tilde{a}_1(x, z)$ and $\tilde{a}_2(x, z)$ do not directly yield the rock properties at a given point, instead the values of $\tilde{a}_1(x, z)$ and $\tilde{a}_2(x, z)$ are of the pertubation in the rock properties at a given point relative to the background medium, see Clayton and Stolt (1981). We will provide images of $\tilde{a}_1(x, z)$ and $\tilde{a}_2(x, z)$ which should map out the regions of changes in rock parameters.

Inversion procedure for $\tilde{a}_1(x, z)$ and $\tilde{a}_2(x, z)$

From the definitions of the $\tilde{a}_1(x, z)$ and $\tilde{a}_2(x, z)$ parameters which we will repeat here.

$$a_1 = \left(\frac{K_r}{K} - 1 \right), a_2 = \left(\frac{\rho_r}{\rho} - 1 \right), \tag{9}$$

we can determine the resulting velocity through the definition of the P wave velocity in an acoustic medium as

$$V_P = \sqrt{\frac{K}{\rho}} \tag{10}$$

therefore solving for K and ρ in terms of a_1 and a_2 and substituting into the expression for the P wave velocity.

$$V_P = \sqrt{\frac{K_r}{\rho_r}} * \sqrt{\frac{a_2 + 1}{a_1 + 1}} = V_{Pr} \sqrt{\frac{a_2 + 1}{a_1 + 1}} \tag{11}$$

V_{Pr} is already known and is the background medium velocity, it is also specified as the velocity of the medium at the surface z=0.

Prior to the deconvolution step we had D' as follows

$$D'(k_m, k_z, k_h) = \frac{-1}{\rho_r} \left[\frac{D'(k_m, k_z, k_h)}{S(\omega)} \right], \tag{12}$$

which demands that we choose an input value for ρ_r, for our simulation cases we choose the value to be set at 1000 kg/m^3. And since V_{Pr} is already set at a value of 2500 m/s the value of K_r is then determined to be 6.75x10^9 Pa. Because all of these values are predetermined we can compute the values of K and ρ at each point and obtain maps of these values from solving for K and ρ

$$K(x, z) = \frac{V_{Pr}^2 \rho_r}{\tilde{a}_1(x, z) + 1} \tag{13}$$

and

$$\rho(x, z) = \frac{\rho_r}{\tilde{a}_2(x, z) + 1} \tag{14}$$

Velocity Models

The models used in this study have been regridded from the original 10m grid to a 5m grid for the reasons mentioned in Young et al (2011). One side effect not initially considered was that the CREWES Matlab routine $AFD\_VELCREATE$ automatically

interpolates velocities into the intermediate cells between two layers if the interpolation creates a grid point between the two known layer velocities.

Hence we actually have an intermediate layer between the intended layers with the intended velocities. The side effect of this should be minimal as the layer itself is only one cell thick, in this case 5m and hence the below the resolution limit of all seismic waves below 100Hz for the model media velocities used here.

Four velocity models are used in this study. They are discussed in more detail in their respective sections but all models are standardized on a 2500m x 1000m grid with 5m spacing, therefore the maximum grid is 500x200 and 100,000 grid point values need to be computed. All models assume a uniform background velocity of 2500m/s and the velocity is homogeneous in the x direction for a given discrete layer for each model. For the irregular and polygonal bodies the interior velocities are uniform as well.

Input Source waveform: the Ricker wavelet

We have chosen a Ricker wavelet as the source wavelet selected at a 20Hz central frequency over 64 or 128 sample points. In all cases the source signature is deconvolved from the synthetic data in order to see what effects, if any, a deconvolution would have on the final results.

Computational Considerations

From the domain of computer science the concept of GIGO (Garbage In Garbage Out) applies to this particular problem and the quality of the input data created by the forward modeling procedures. In computational problems there is always a trade off between accuracy and the time needed to obtain the result. In our case with 10^5 grid points (500x200) to be computed per shotpoint and 500 shotpoints/group and 40-60 offset groups, the forward problem alone consumes 15% of the total run time, averaging 3 hours to generate a single synthetic data set for a single velocity model.

The migration step itself takes around 600-800 minutes of time to complete(around 10-13 hours) and so there is going to be a large trade off between having accuracy and having computational efficency. These times are for execution on a six core Intel PC running parallel MATLAB on all cores and nothing else. Extensive parallelization of this program is one possibility and has been attempted without much success within the Matlab environment, mainly due to the author's lack of experience in parallel computing. These simulations are not considered realistic in terms of the length and depth coverage

F-D stability

We discussed grid dispersion effects if the incorrect grid spacing is chosen for the forward modeling step in the first paper. One effect observed was the problem with an overlap feture seen in all images in the central region, at 10m grid spacing this was clearly apparent but disappears at the 5m spacing.

There is a lower limit to the grid size before other FD effects take over such as grid overrun, where the speed of propagation on the grid is so fast it causes errors in the accurate location of the wavefront Bording and Lines (1997). For our case the expression in 2D is

$$c_i(z)\delta t * (\sqrt{\frac{1}{8}} or \sqrt{\frac{3}{8}}) = h \tag{15}$$

where δ t=0.5ms and h is the minimum step size of the grid to maintain stability, our max. model velocity used is 6000 m/s which corresponds to h=4.2 m for a 2nd order Laplacian approximation or h=1.83m for a 4th order Laplacian, these are the minimum grid spacings and is less then the 5m spacing used in our models so we won't suffer from this issue. A possible solution is to implement the use of a sixth order Laplacian FD routine which allows for a smaller grid spacing and high contrast in model velocities as well. This comes at the cost of additional computational time which is the trade off needed to higher accuracy.

SYNTHETIC EXAMPLES

We have chosen to test our inversion process using four cases. A single horizontal reflector with a large velocity contrast between them. A four layer model with constant horizontal velocities in each layer but different from layer to layer. A "shallow" body containing low velocity material intruding into a 4 layer model background which contains a concave top surface and a convex bottom surface. Finally, a case where again there is an intrusion into a background four layer model but this time the body has a strongly concave upper surface and a convex lower surface containing higher velocity material than the surroundings.

For these experiments we have fixed the model parameters at a receiver line length of 2500m and a depth of 1000m (corresponding to a time of approximately 0.8 sec), we then choose a source/receiver spacing of 5m and a sampling time of 4ms. For the forward differencing calculations the time step is 0.5ms between frames and a computation grid of 5m in the x direction and 5m in the z direction. A bandlimited source wavelet was also added which in this case is a Ricker wavelet with a user specifiable frequency and duration, we used 20Hz and 128 samples.

For each case the initial velocity model is used as input into the CREWES forward differencing routines and are displayed for each model run. In the four layer case this is followed by a snapshot at one particular source point comprising the gather of the receivers for that source point. A deconvolution was then done on all the shot profiles and a single snapshot is displayed, usually at the same source point, the displayed image is also missing the direct wave as this was subtracted prior to the deconvolution.

The computation of the k_z, k_m grid is needed to sample enough of the k-space grid to give the proper resolution and details. Initially we found that sampling only the points in quadrant 1 $(+k_z, +k_m)$ produced inversions which were incomplete, only reflectors with a positive slope were imaged and the structures with a negative spatial slope were absent. When we sampled k-space quadrant 4 $(+k_z, -k_m \rightarrow 0)$ plus quadrant one $(+k_z, 0 \rightarrow +k_m)$ we were able to obtain a complete and structurally correct migration.

To do a proper inversion required computation of migration images at two or more half-offset values, k_h. Once this is computed then a least squares inversion is done using the algorithm used to compute a_1 and a_2 given above, an image in k_z, k_m space is produced prior to inverse Fourier transforming back into x,z space.

The shotpoint images were scaled using mean value and not max value scaling to bring out the details of each of the models and results. Max value scaling produced images with a bright spot at the top, where the wave amplitudes from the shot is the greatest and the rest of the image was too faint to clearly see the details due to geometric spreading.

RESULTS FOR A 1-D MODEL

A simple 1-D model will illustrate many of the features we will be looking for in an accurate inversion, as can be seen in fig.1 if the synthetic input data has the complete spectrum of frequencies from 0Hz to the Nyquist limit then the integration of the trace will produce a fairly accurate stepped function profile. The main feature is that the first discontinuity location corresponds with the expected location of the first interface.

Subsequent discontinuities will not match up in depth due to the fact that the inversion formula uses only the first layer velocity, Bleistein et al. (2001) has a through explanation on the reasons for the cumulative errors in depth below the first interface, this effect is seen clearly in the 1.5D and 2D models.

The amplitudes of the step function should correspond approximately to the ideal step function amplitudes and it does for the first interface as can be see in fig.2 A major effect is illustrated in these figures, when the frequency range becomes bandlimited we get very strong deviations from the step profile. A loss of the 0 Hz frequency causes the horizontal parts of the step to deviate strongly, as can be seen in the frequency plots, this is expected as the idealized step function is an infinitesimal sum of all possible frequencies. The loss of high frequencies introduces a Gibb's phenomena into the trace integration causing a high frequency oscillation in the sharp corners and a overshoot at the corner itself.

The progressive loss of frequencies doesn't affect the location of the interfaces in the integrated trace nor the amplitudes but it does cause the profile to tend towards resembling the plot of a series of delta function spikes with average amplitudes tending to zero in between the spikes. As we will see later this effect is very strong in the synthetic data for various models. One major advantage of 1D models is that there is no geometric dispersion effect to take into account in the amplitudes.
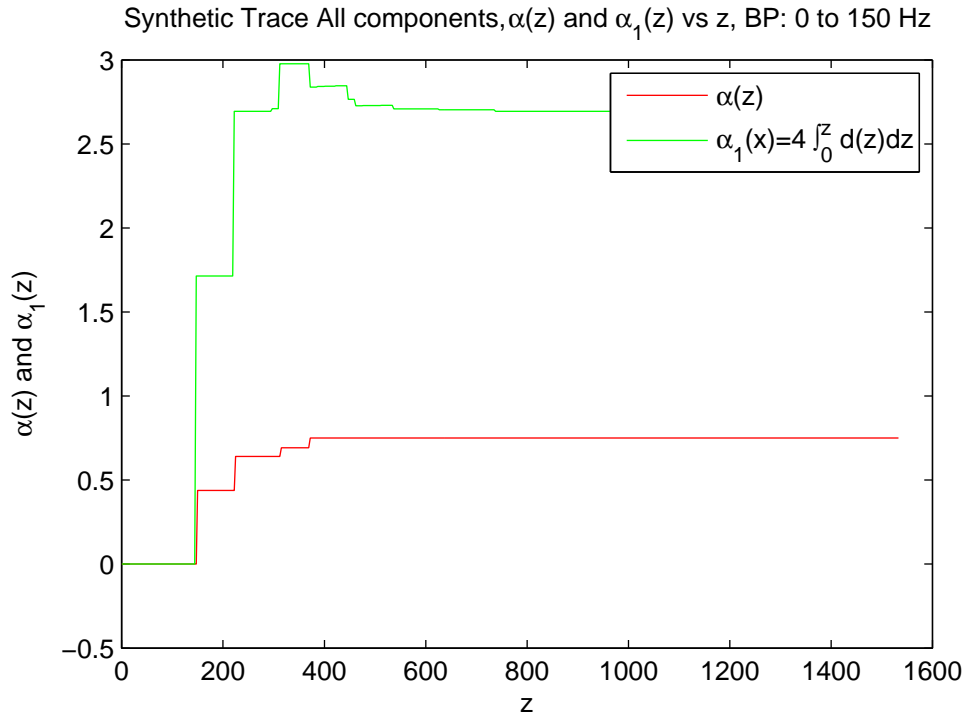
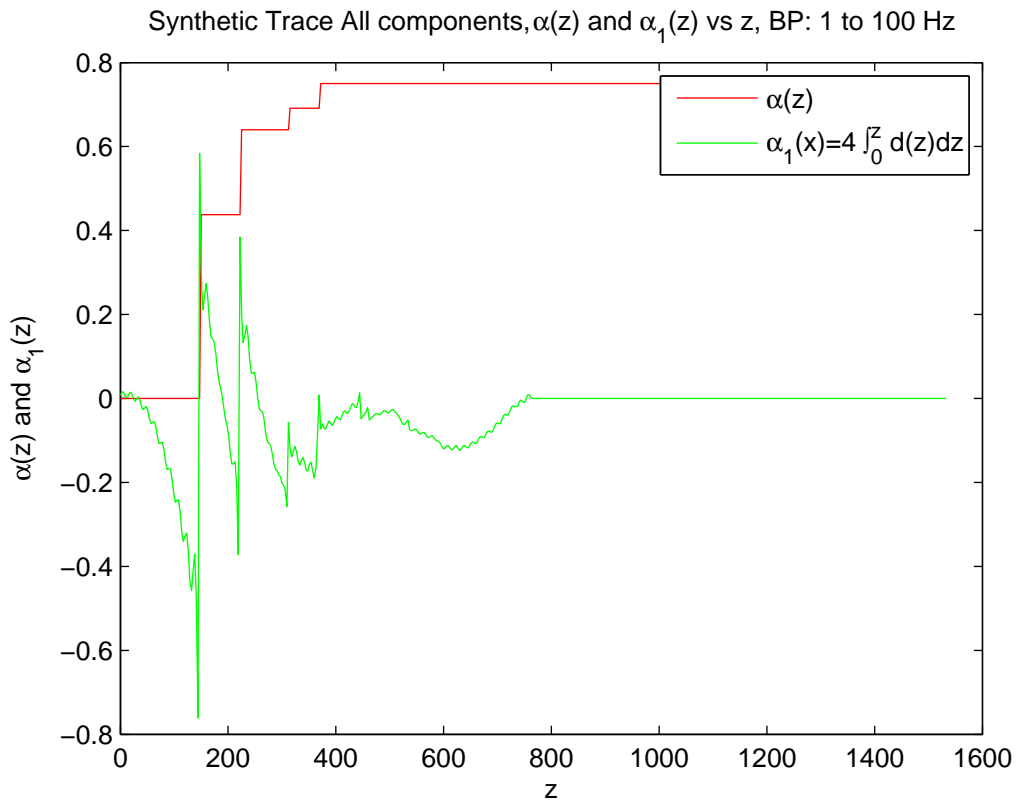FIG. 1: Plot of the model velocity profile α and the integrated trace α_1 between 0 and 150 Hz

FIG. 2: Plot of the model velocity profile α and the integrated trace α_1 between 1 and 150 Hz

RESULTS FOR 1.5-D MODELS

A 1.5D model is defined to be a model which has a heterogeneous velocity profile only in depth, the velocity does not vary in the horizontal direction. This type of model can retain the normal incidence assumption of a 1-D model while testing in a pseudo 2D environment, ie horizontally extending a vertical profile.

The 2 Layer high velocity model

This two layer model (fig.3) is done as a simple test to determine if a large velocity difference has the expected effect on the resulting pertubations in the rock properties. Figure 4 shows the migrated result of the model run and looks as expected. The velocity difference across the interface is 1500 m/s so the reflection coefficent is quite large. A small step is present in the middle of the image and is 1 grid cell(5m) in height, this was done to see if the step is present in the migrated data and to determine the effects on the pertubation maps.

After the inversion stage we have two pertubation maps as shown in figure 5 and figure 6, the model run used k_h=80 half offsets whereas the 4 layer model case used 20 offsets initially. This has produced an effect mentioned in Clayton and Stolt (1981) which is now noticeable. The relative intensities of the two properties are beginning to differentiate each image from the other, the relative maximum value for the bulk modulus image is in fact 55, where as the maximum value for the density image is 70, the two images have been rescaled equally to illustrate that the relative weighing of intensities have shifted and this is expected as more information in the form of more offset data was included into the inversion.

The last figure in this section (fig.7) displays the level of pertubation from the background velocity field for the two layer model. As expected where there is no interface between the two layers there is little change from the background velocity of 2500 m/s(yellow in the image), ignoring the false high frequency variations. Where the interface is located the amplitude decreases to around 1000 m/s(blue areas), this is a difference of 1500 m/s which is the magnitude of the difference found on the initial velocity model not accounting for the sign change. To save space the images of the K and ρ pertubations in absolute units have been omitted due to space limitations for this simple model.
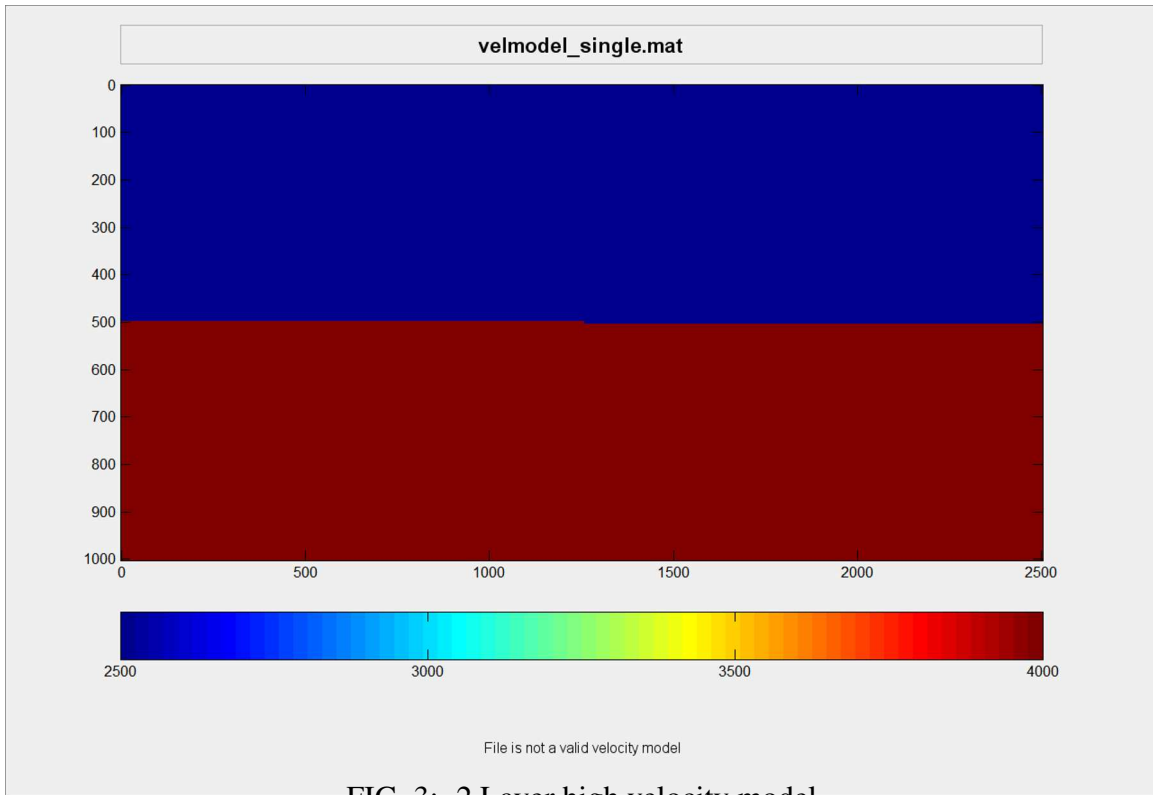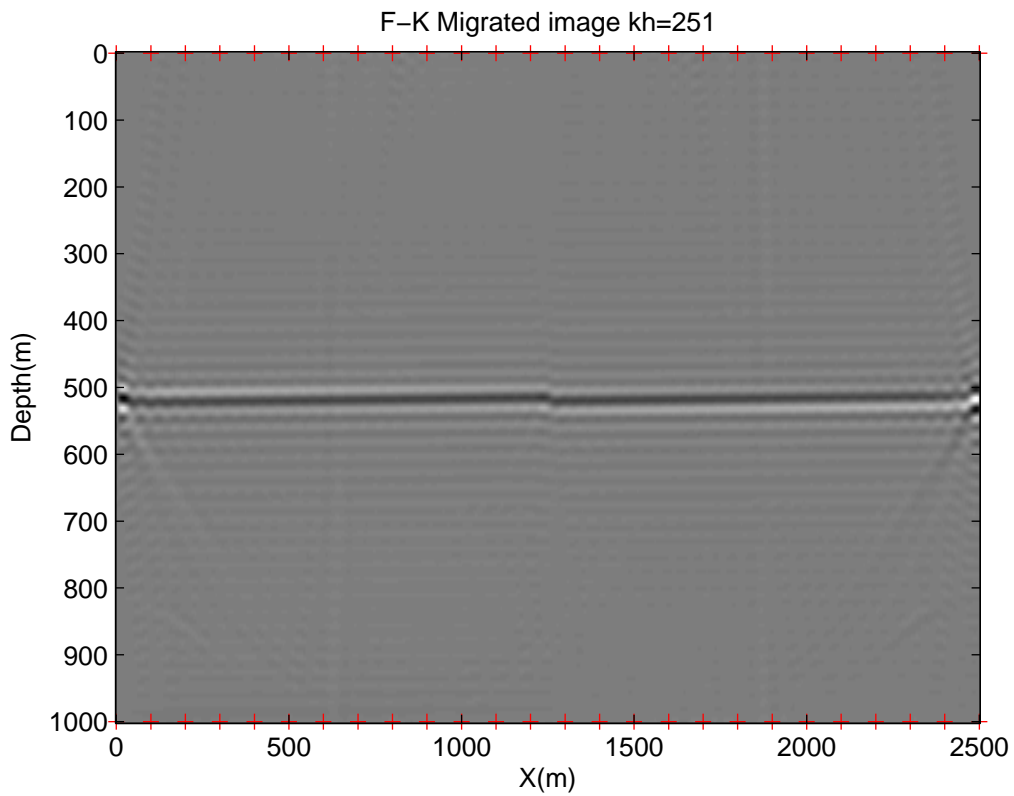
FIG. 3: 2 Layer high velocity model

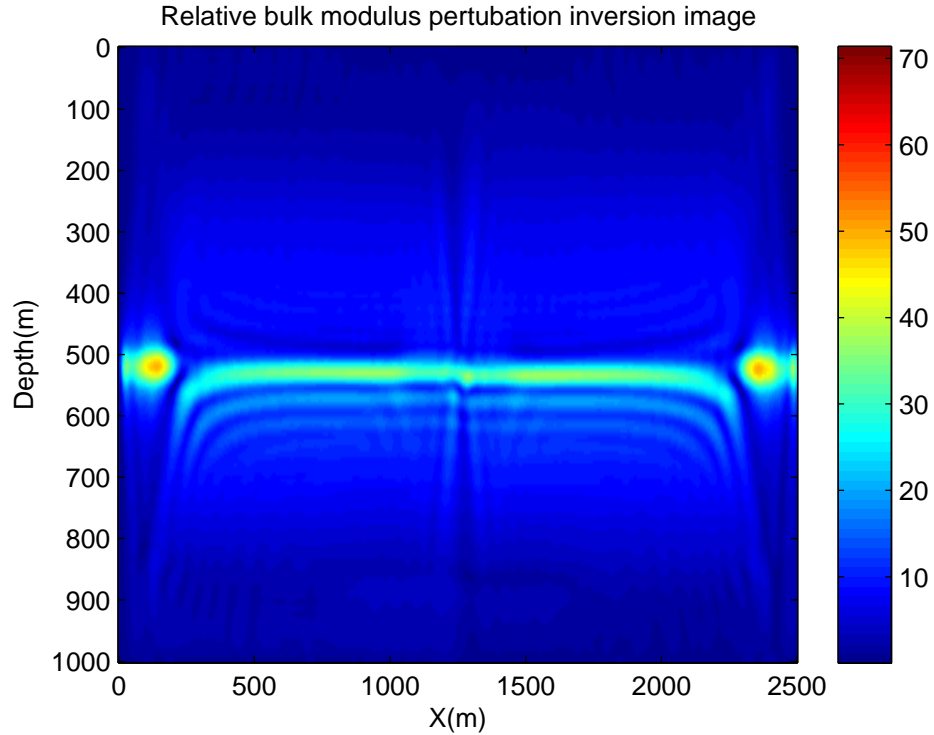FIG. 4: 2 Layer high velocity model, deconvolved synthetic data, x=1195m

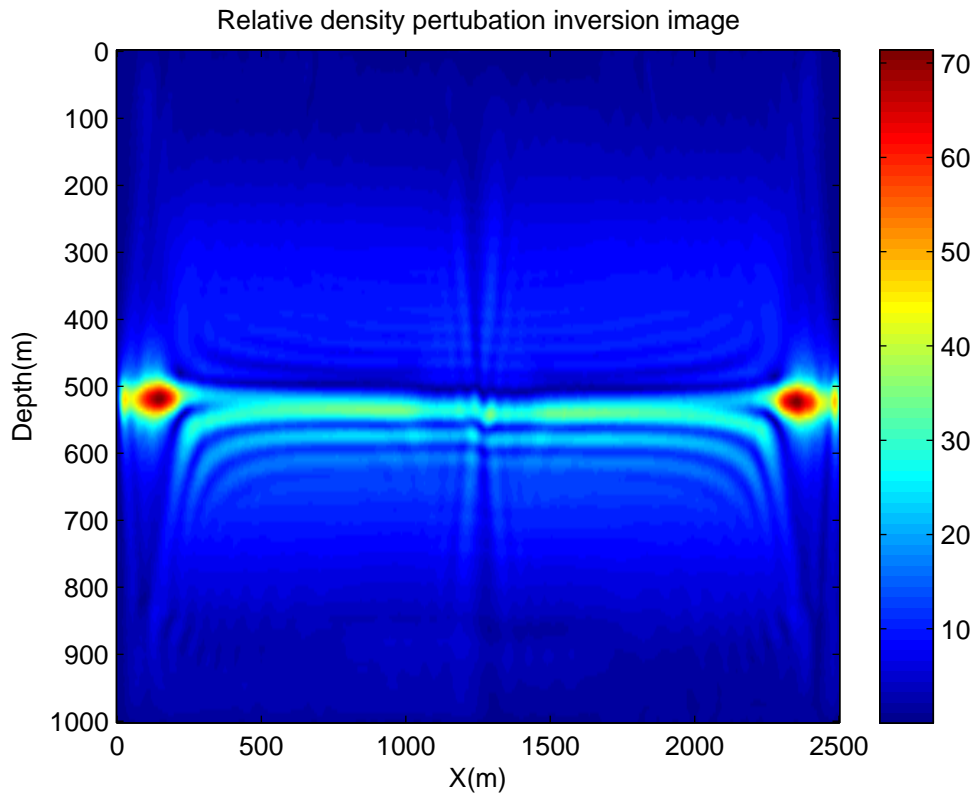FIG. 5: Inverted bulk Modulus pertubation image for a 2 layer high velocity model

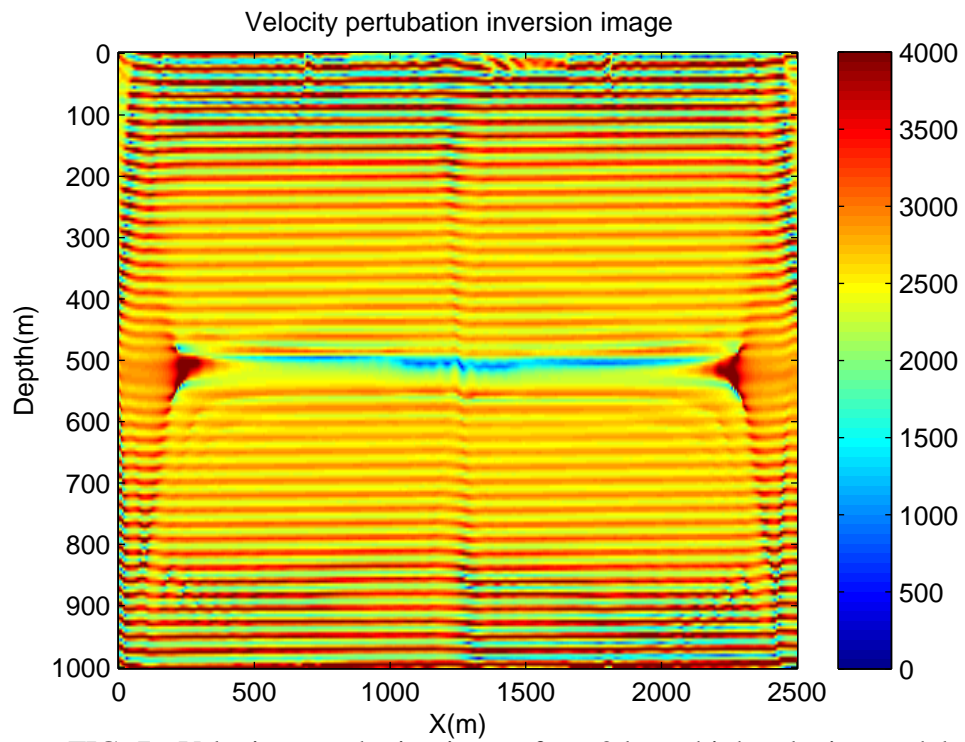FIG. 6: Inverted density pertubation image for a 2 layer high velocity model

FIG. 7: Velocity pertubation image for a 2 layer high velocity model

The four layer horizontal model

This physically simple model is relatively more complex then the 2 layer model and demonstrates the power and accuracy of the inversion routine, in figure 10 and figure 11 we get the expected responses from the forward differencing model. Hyperbolic features corresponding to the model reflectors and in the deconvolved case as in all cases we've subtracted the direct wave. We do get some high frequency "wakes" following each of the hyperbolic returns plus reflections from the sides of the aperture. Note the z axis is labeled in time, this is because of the output of the particular CREWES plotting routine used and in which there wasn't time to change over to a depth labeled axis.

In Figure 12 we can see a very simple one dimensional column in k_m, k_z space, this is because there is only the horizontal reflectors which are flat and so no variance in relative angle the source and no "slope" their a straight vertical column is expected. Figure 13 shows the resulting migration, again we have some wakes and aperture artifacts on the sides. But we do get the expected number of layers with reflector 1 at the model depth expected.

The difference is in the depth of the second and subsequent layers. Reflector 2 and 3 are shallower then expected because there is a difference in layer velocities which are not accounted for in the inversion algorithm below the first reflector. This is due to the number of terms in the Born approximation that we take. This effect will be apparent across all the models we choose to use.

The 4 layer migrated data is then processed through the inversion stage, figures 14 and 15 are the result after the fourier transform is performed to move from the wavenumber k_m, k_z) to the space domain (x,z). What is displayed is the pertubation in the physical rock properties, bulk modulus K and density, ρ, relative to a uniform background medium. The colorbar scales are relative units. As can be seen, the reflection boundaries clearly show up as discontinuties in the medium, the amplitude of each deeper layer increases because the relative velocity differences increase by 500 m/s from the previous boundary, ie the background velocity is 2500 m/s, jumping to 3000, 3500 and 4000 m/s at the last interface.

Aside from the hotspots at the sides of the reflectors the images are fairly smooth within each layer because of the least squares minimization process which acts as a smoothing filter and minimizing the noise in the final image. In this case 40 migrated images were calculated for a range of half-offset values, k_h between 231 to 271 out of a possible 500 values.

This small spread of k_h range is not enough to begin to distinguish differences between the K and ρ images as has ben pointed out in Clayton and Stolt (1981). In a later model we will see differences when the spread of k_h is increased and other side effects from a large number of offsets being used.

Figures 16 and 17 display the result of applying equations 13 and 14 using the calculated pertubation parameters $\tilde{a}_1(x, z)$ and $\tilde{a}_2(x, z)$. The pertubation magnitudes are not large relative to the mean property, for instance the background density, ρ_r is set at 1000 kg m^3 and the highest pertubation in density is almost at 1100 kg/m^3 which is a 10% differ-

ence. The same applies to the bulk modulus map as well. Both images also display the high frequency horizontal artifacts present on the original migrated image which are of course not real variation in the physical medium.

The final figure 18 shows the result of computing the P wave velocity of the medium using eqn.18, the velocity changes are of the correct sign but of much lower value then anticipated and will need to be further investigated.
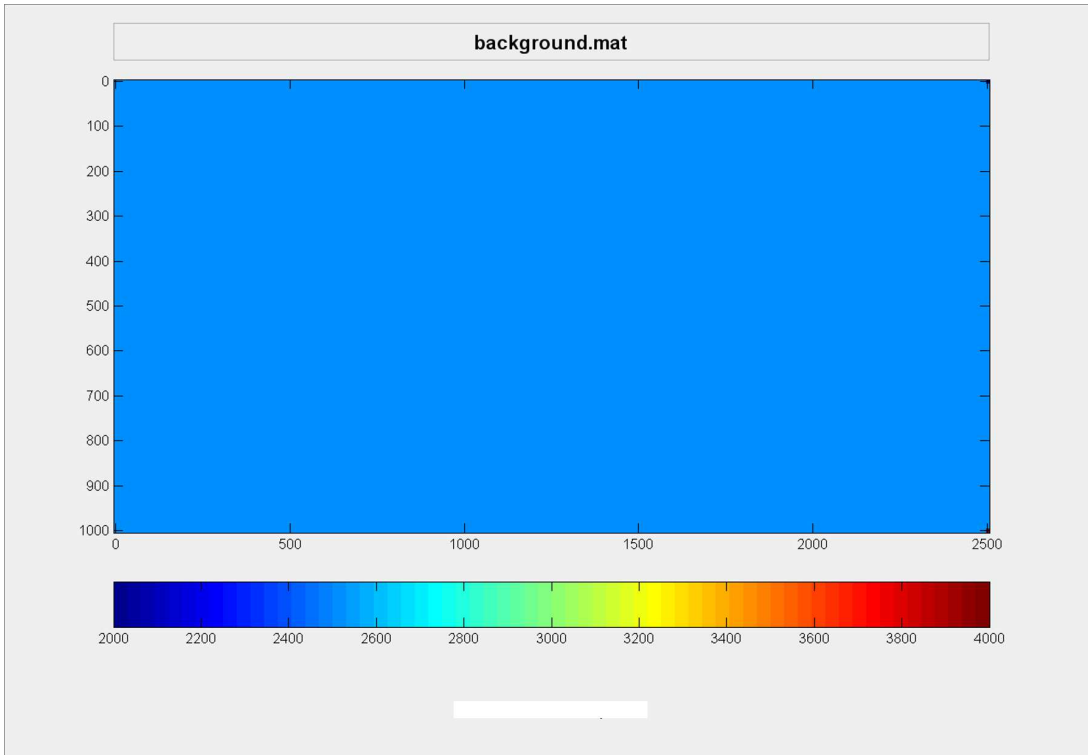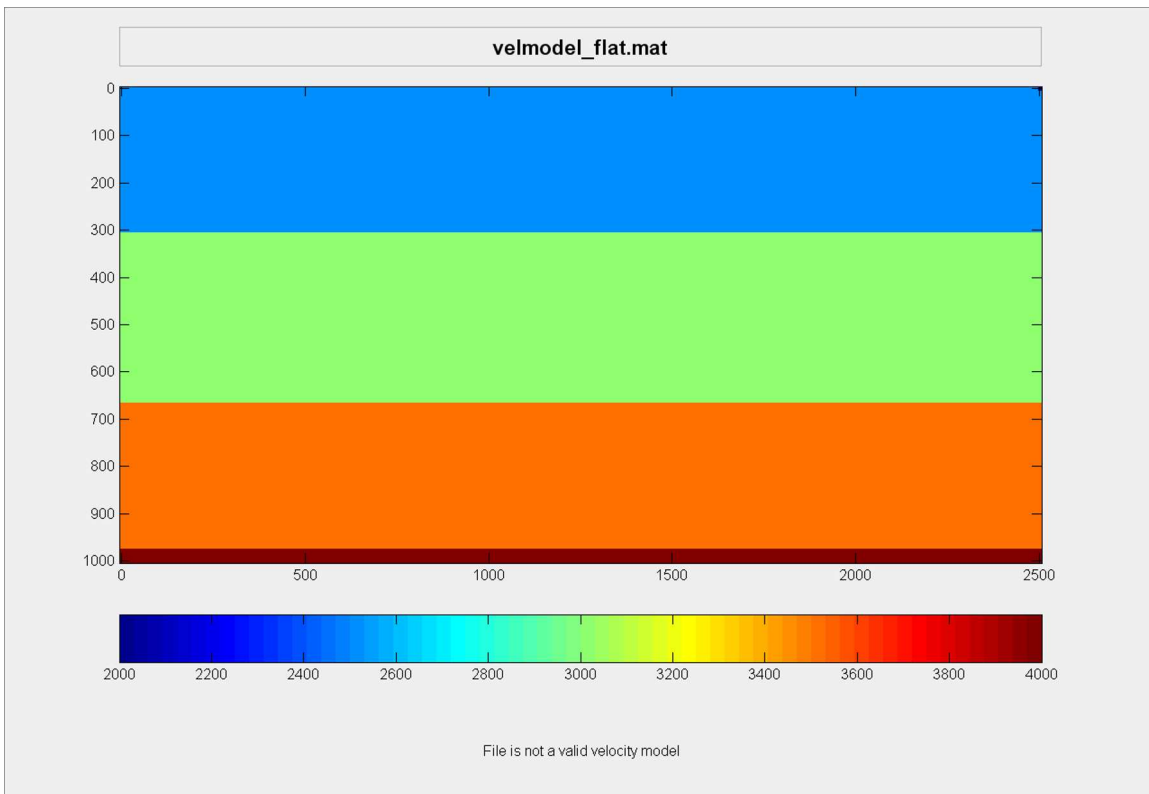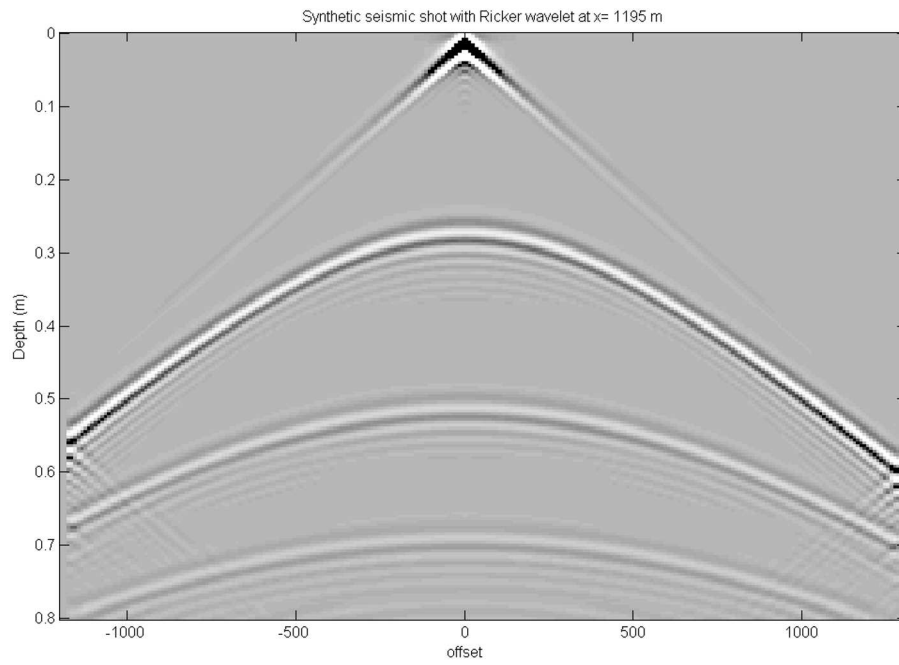
FIG. 8: Background velocity model

FIG. 9: 4 Layer flat velocity model

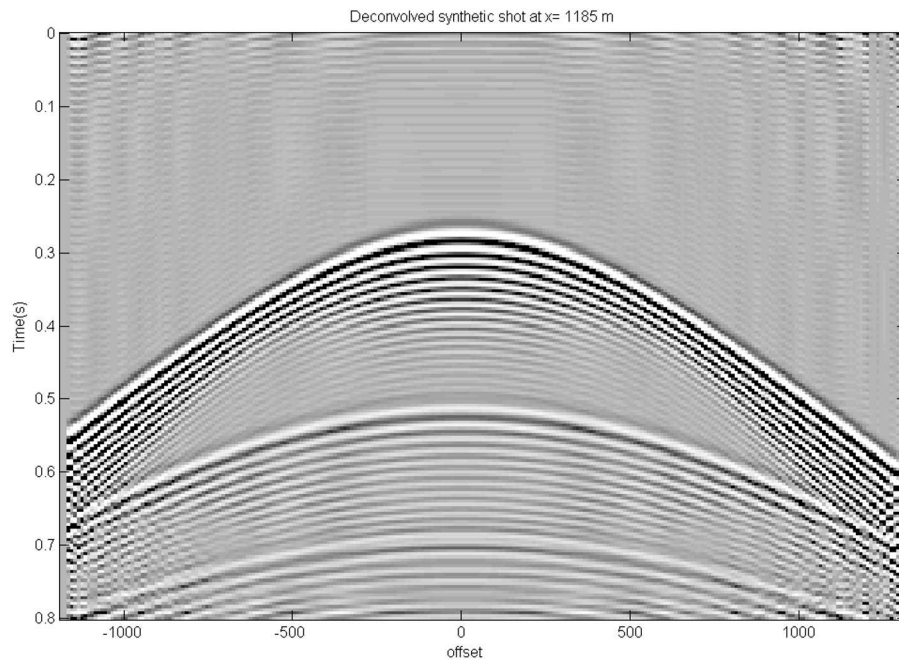FIG. 10: 4 Layer flat velocity model, synthetic data with 30 Hz ricker wavelet, x=1195m

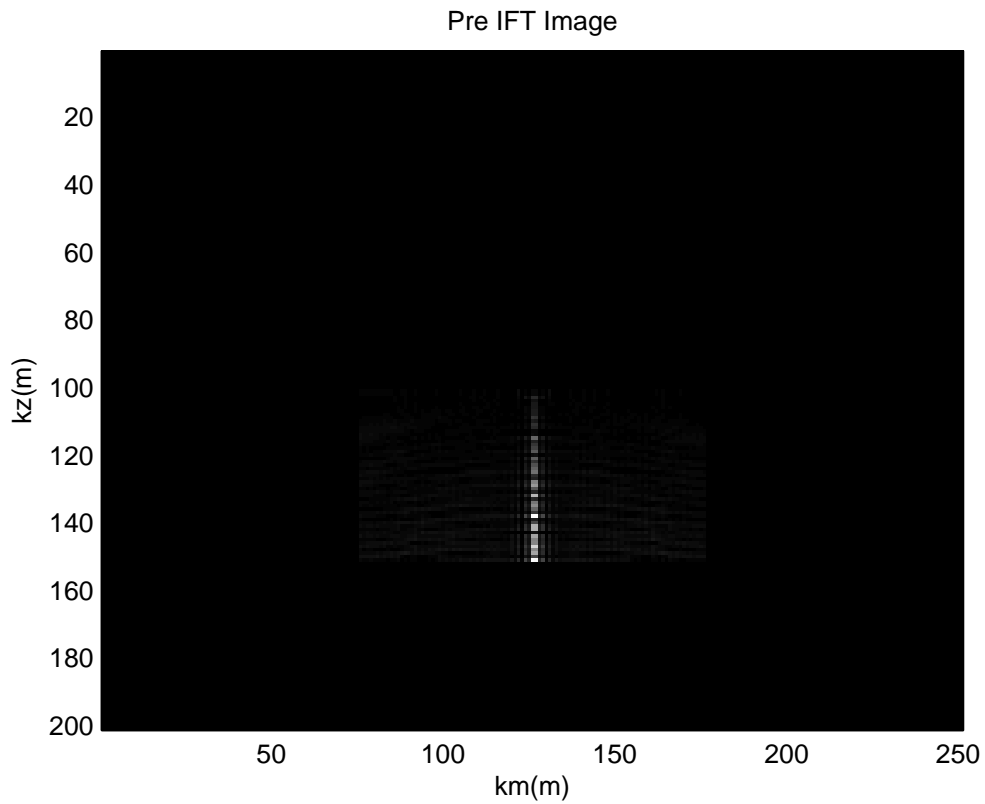FIG. 11: 4 Layer flat velocity model, deconvolved synthetic data, x=1195m

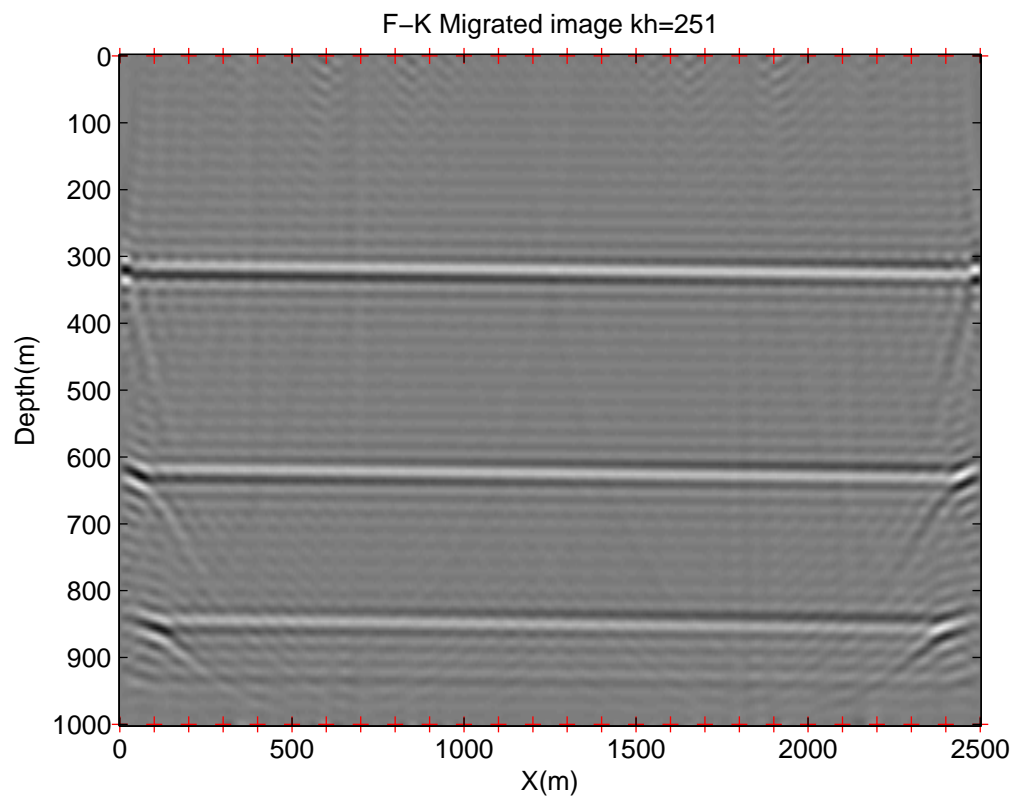Pre IFT Image

FIG. 12: 4 Layer flat model k_z k_h plot

F–K Migrated image kh=251

FIG. 13: 4 Layer flat velocity model, deconvolved, migrated synthetic data, x=1195m

Relative bulk modulus pertubation inversion image

FIG. 14: Inverted bulk Modulus pertubation image for a 4 layer model

Relative density pertubation inversion image
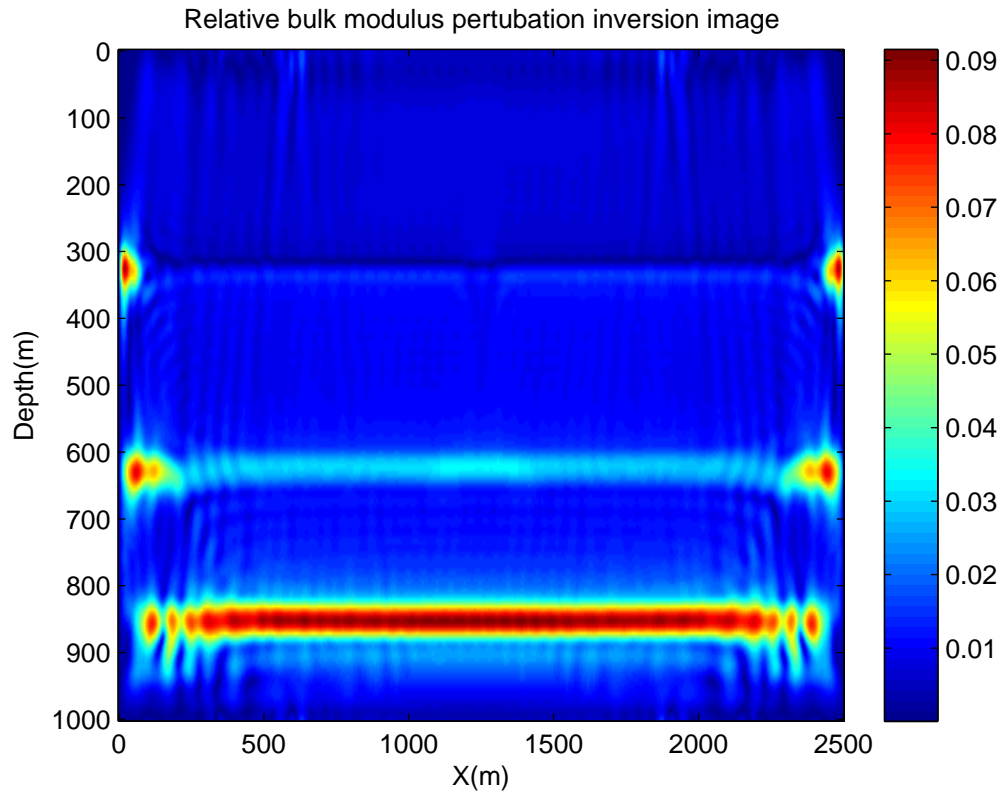
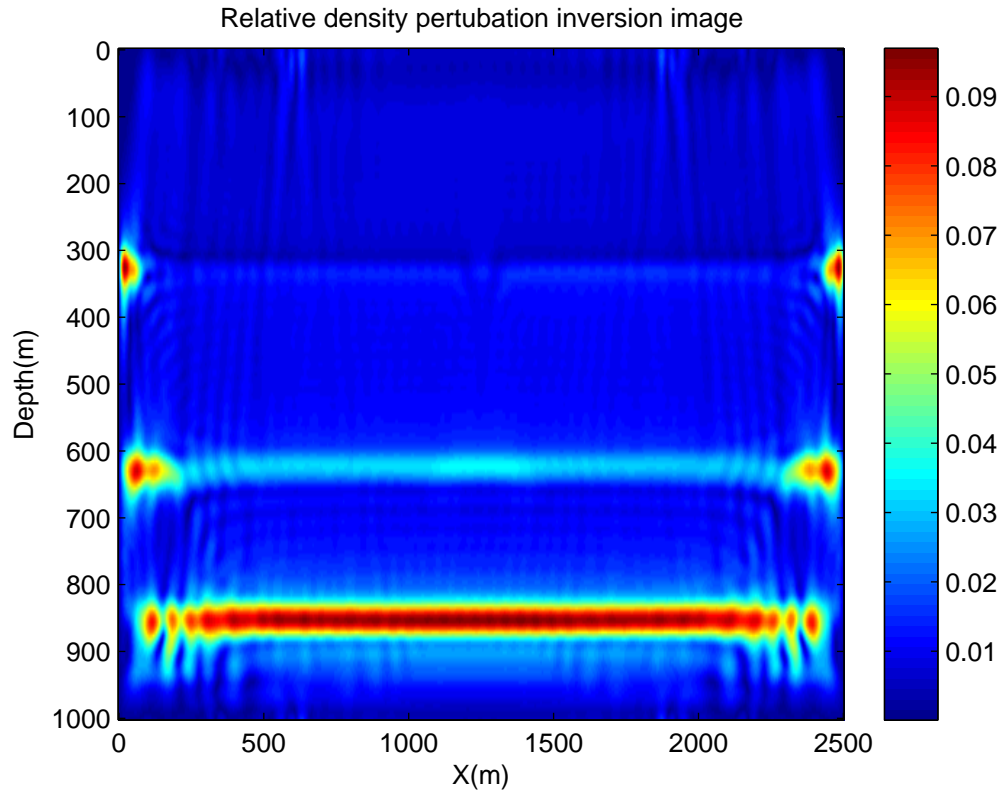
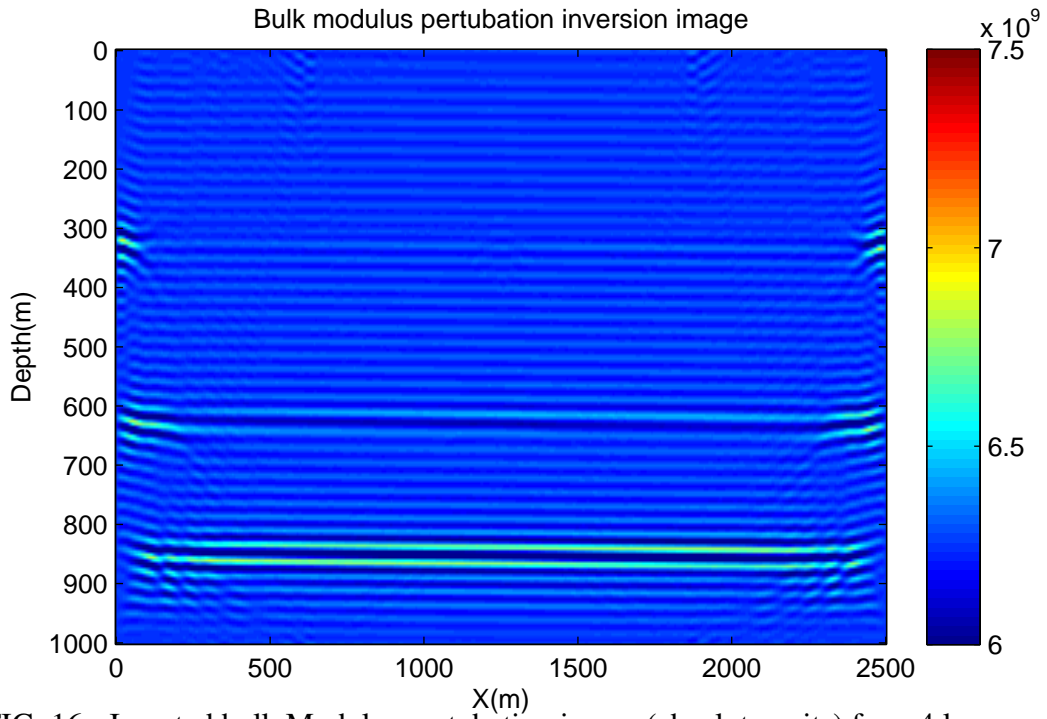FIG. 15: Inverted density pertubation image for a 4 layer model

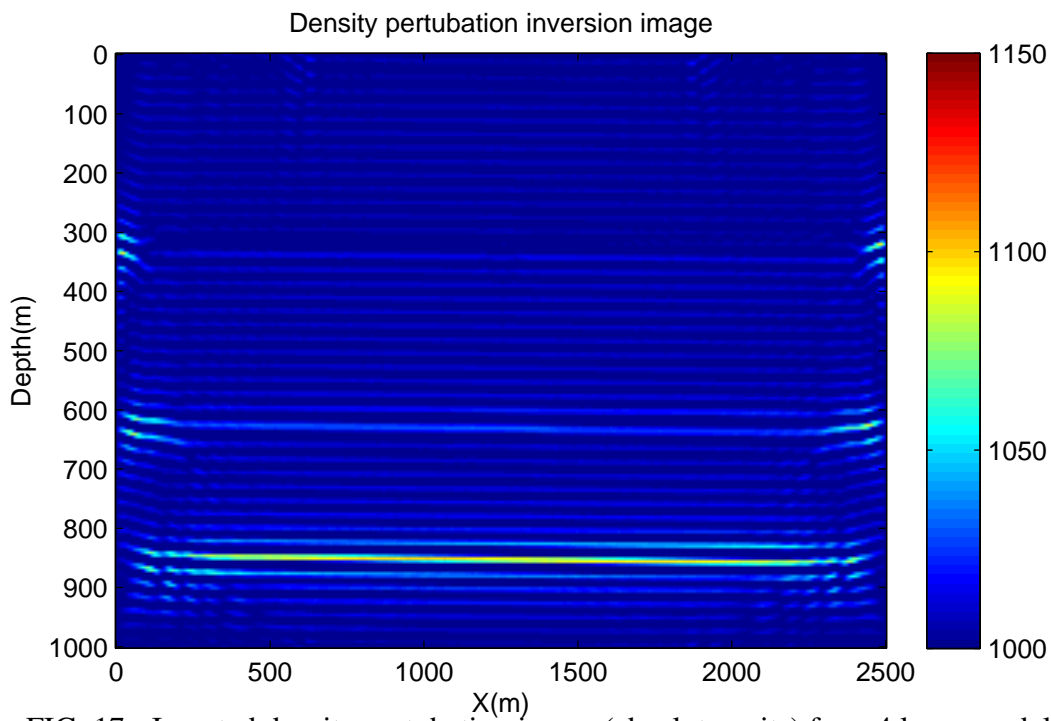FIG. 16: Inverted bulk Modulus pertubation image (absolute units) for a 4 layer model

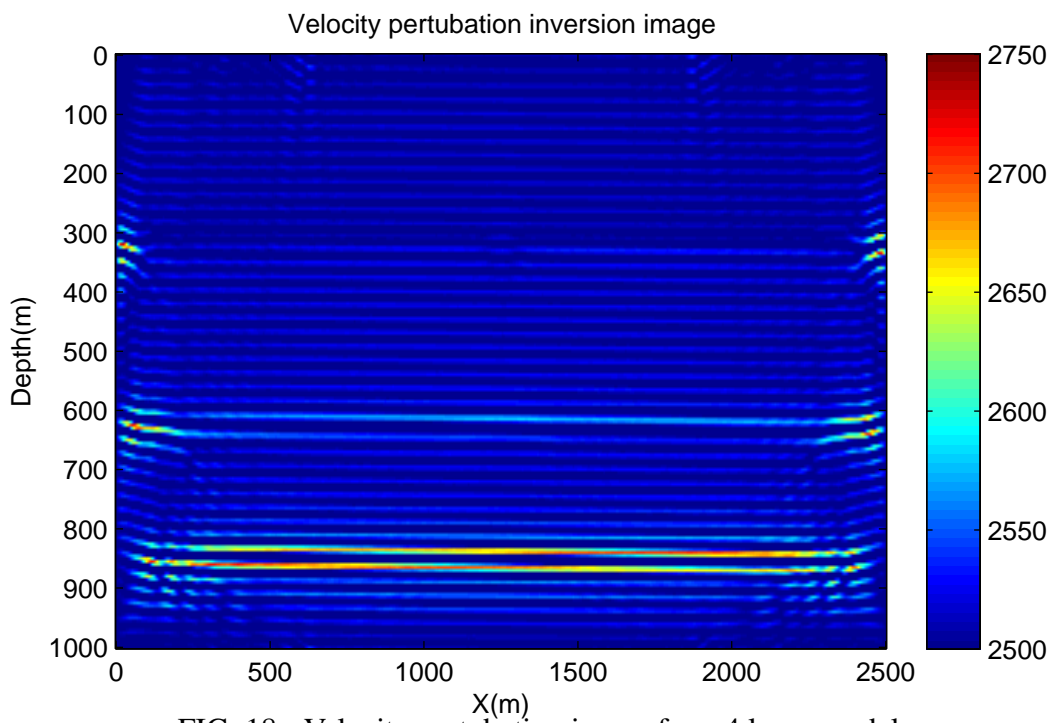FIG. 17: Inverted density pertubation image (absolute units) for a 4 layer model

FIG. 18: Velocity pertubation image for a 4 layer model

RESULTS FOR 2-D MODELS

Two fully 2D models are analyzed here to check for differences from the 1.5D models in terms of observed effects and any additional effects not observed in a 1.5D domain.

The shallow low velocity model

The shallow, low velocity model shown in fig.19 was created to see if the inversion properly handles the deep reflectors when encountering a low velocity layer. In this case we have a biconvex lens embedded in a four layer model. The four layer background is the same as discussed in the previous section, only the addition of the low velocity body is the difference. Going through the standard processing procedure we can see the results of the deconvolution and migration in figure 20. The migrated image displays the expected features, the low velocity of the body distorts the traveltimes of waves passing through it. This has distorted the apparent position of deepest interface as seen in the migrated image. There are numerous low amplitude artifacts present, some of which are reflection multiples, especially ghost images of the body itself.

The lower convex part of the intrusion is not located in exactly the correct depths due to the velocity difference, this can be seen in the migrated image. Note the deformation of the lowest reflector layer at z=850 m depth in the model and how it distorts from a horizontal reflector in the model into a concave shape, due to the distortion in travel times introduced by the low velocity found in the intrusion. Details of the velocities can be found on Table 2 of Appendix A.

Inversion of the migrated images are shown in figures 21 and 22, again both images look to be almost exactly the same but the amplitudes are different enough to be noticeable. The boundary around the low velocity zone provides a strong contrast to that of the surrounding layers, in fact the P wave velocity of the body is 100 m/s lower then the background medium. There is significant bright spot in the middle of the deepest reflector just under the midpoint of the low velocity body which is not straightforward to explain but maybe due to refraction effects of waves impinging on dipping surfaces.

The final image (fig.23) is of the pertubation in the velocity field, the outline of the low velocity zone shows up clearly as much stronger then all but the deepest horizontal interface. There is a very large amount of noise in this image which makes it difficult to quantatatively discuss the results.

In the inversion images there is a noticeable 'beading' effect, which is a series of bright and dark spots along the interface, this occurs in both 2D models displayed here. This occurs where there is a sharp corners in the model, as can be seen in fig. 19 along the sides of the model is a jagged line and is an effect due to the gridding of the model. The interface boundaries cannot be interpolated below the resolution of the grid and so the position of the line is approximated. These rough edges act as point diffractors and can cause interference patterns to be created in the image as can be seen in the interior of the body where the velocity should be uniform.
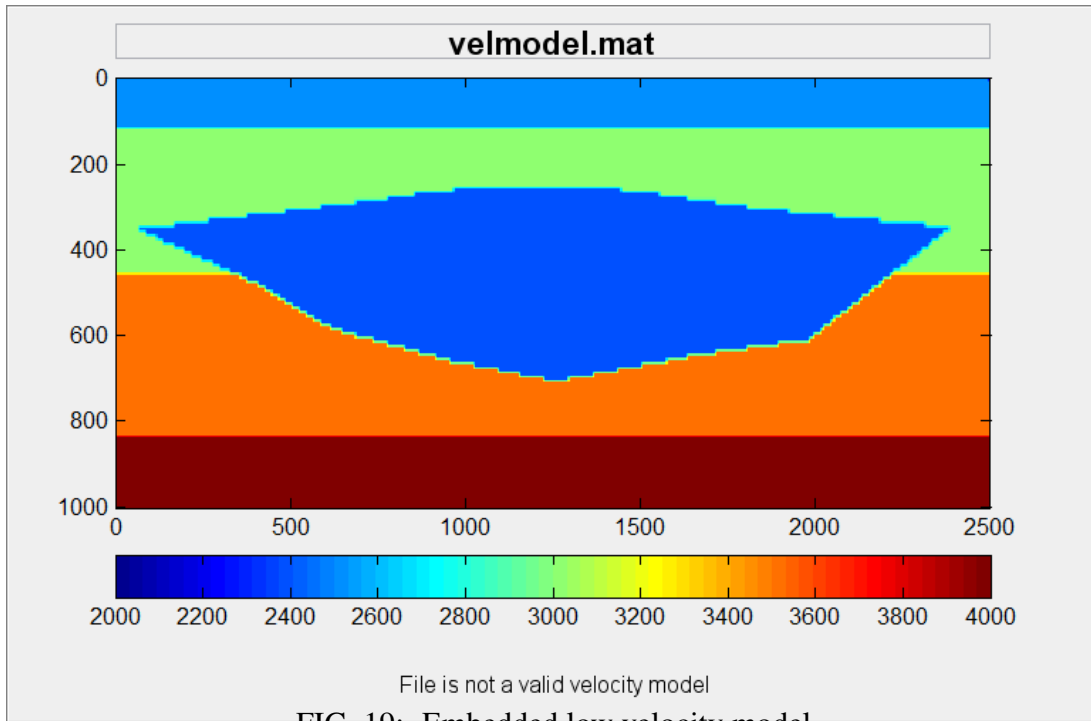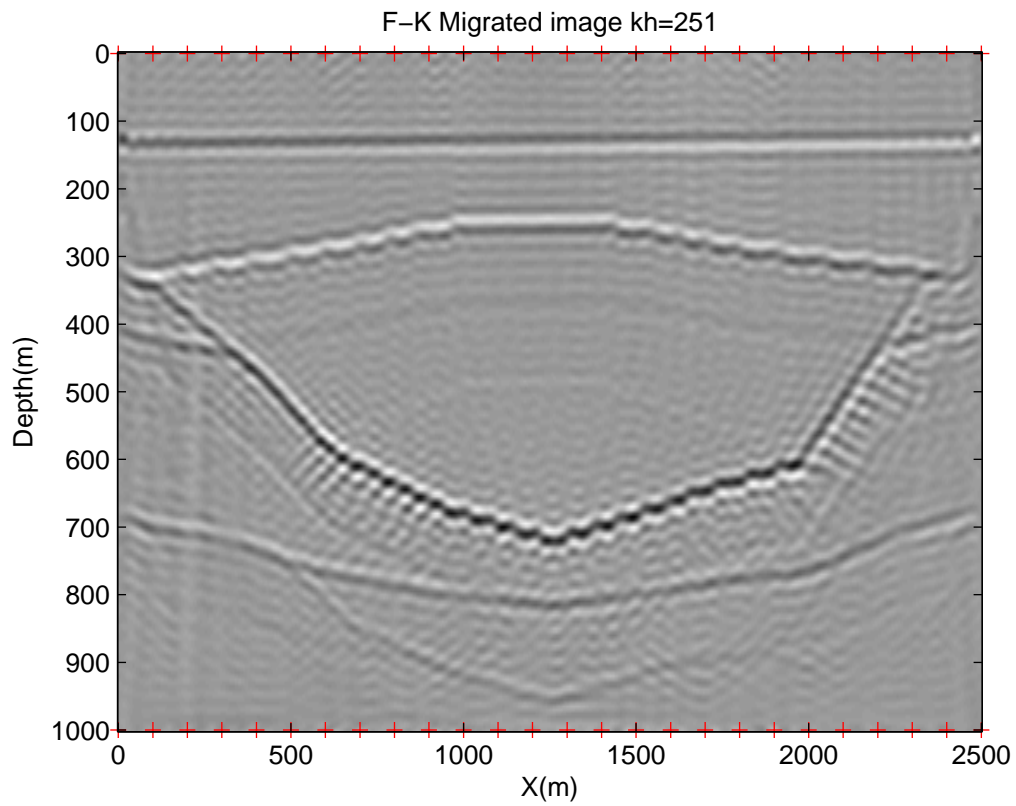
FIG. 19: Embedded low velocity model

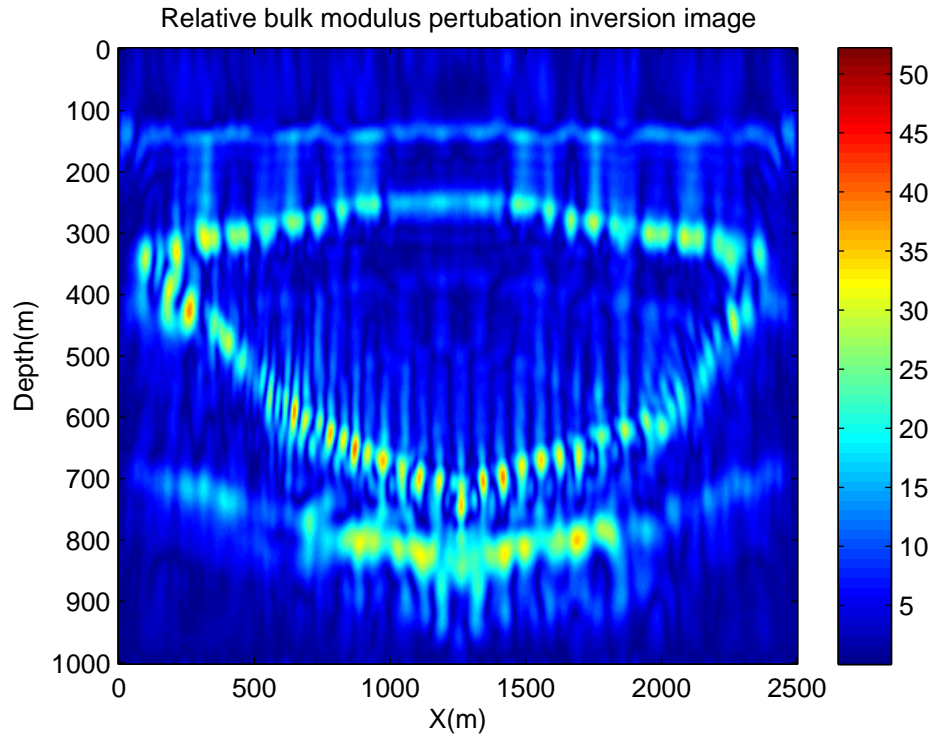FIG. 20: Embedded low velocity model, deconvolved, migrated synthetic data, x=1195m

FIG. 21: Inverted bulk Modulus pertubation image for a embedded low velocity model
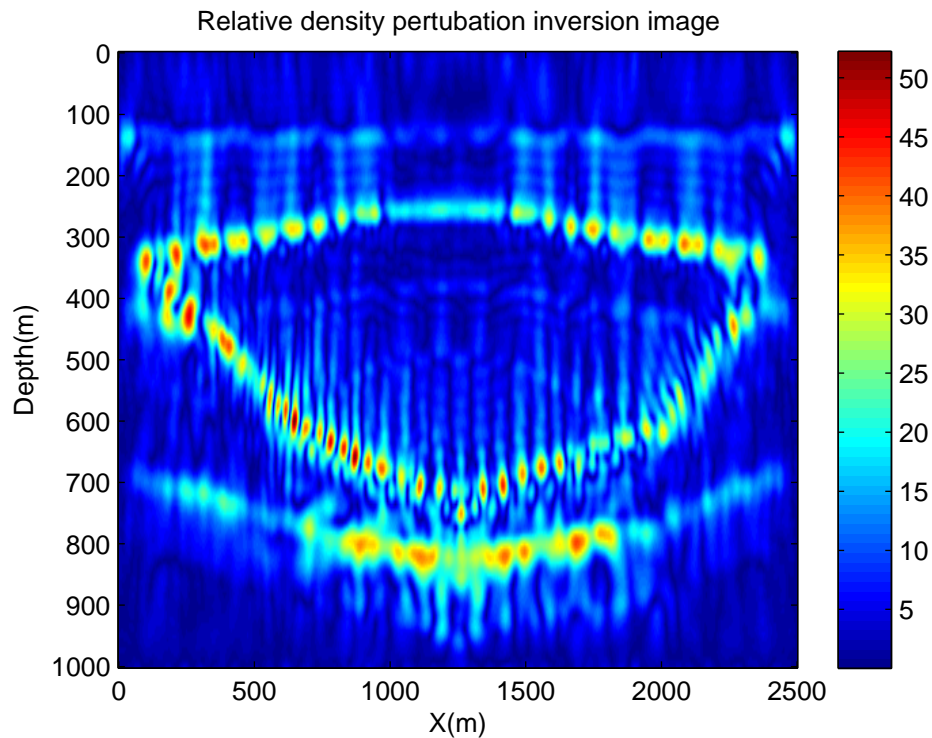

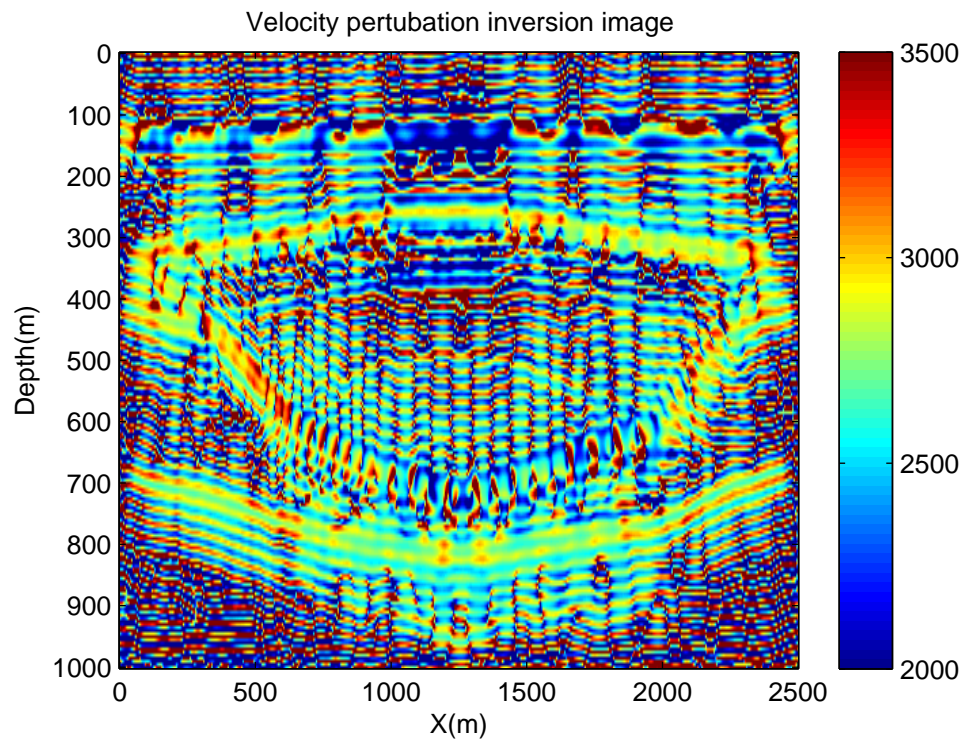FIG. 22: Inverted density pertubation image for a embedded low velocity model

FIG. 23: Low velocity body pertubation image

The Anticline velocity model

The anticline velocity model shown in figure 24 also has a low velocity center relative to all but the top two layers. With a gradually increasing dip to the concave upper surface and a convex lower surface this model should create significant distortions and be challenge to image. Again the four background layers are the same velocities as found in the 1.5D 4 layer velocity model. The internal velocity of the body is 3200 m/s which is higher then the background medium and different from the case given previously.

The sides of the upper surface have a greater slope towards the ends while the lower surface has a fairly consistent and shallower angle. The steep dips on the upper side means we see a gap in the migrated image on the lower left and right sides wings. This is indeed the case as seen in fig. 25, there is also a significant amount of noise associated with multiple reflections and diffraction features from the edges of the layer interfaces.

Figures 26 and 27 show the results of the inversion carried out on the migrated data, notice the pertubation features outline the model velocity structure quite well and most of the artifacts are absent, even the multiples are not very strong in amplitude compared to the primary pertubation features. Again as in the other models their is a slight difference in relative maximum amplitudes between each image. These inversion images were computed from 40 k_h half-offset values

The next set of images shown in figures 28 and 29 illustrate a point made in the figure 2 caption of Clayton and Stolt (1981), about the region of resolution of bulk modulus and density variations. In these cases k_h has been increased from 40 to 120 half-offset images, this was done to see if there were clear distinctions between the bulk modulus and density pertubation results. As can be seen there are clear intensity differences favoring density changes over bulk modulus changes.

What was not taken into account when this simulation was run is that the ratio of k_h/k_z needs to be maintained. In our case the k_z was fixed at 50 wavenumbers, for the original run we have a ratio of 40/50=0.8 for the next run it becomes 120/50=2.4, this produced a very strong resolution effect which moved the resolution limit to shallower depths. It's why the greatest intensity region seems to be focused at the 350m level instead of the 700m level.

The change occured because the source-reciever offset appears to have increased relative to the depth of the reflector, favoring in our case the shallower reflectors. As the images shows all the features visible in the prior images are still present but look much weaker at depths greater then 350m. The solution would have been to maintain the k_h/k_z ratio and increase the value of k_z from 50 to 150 wavenumbers but will greatly increase the computational time as well.
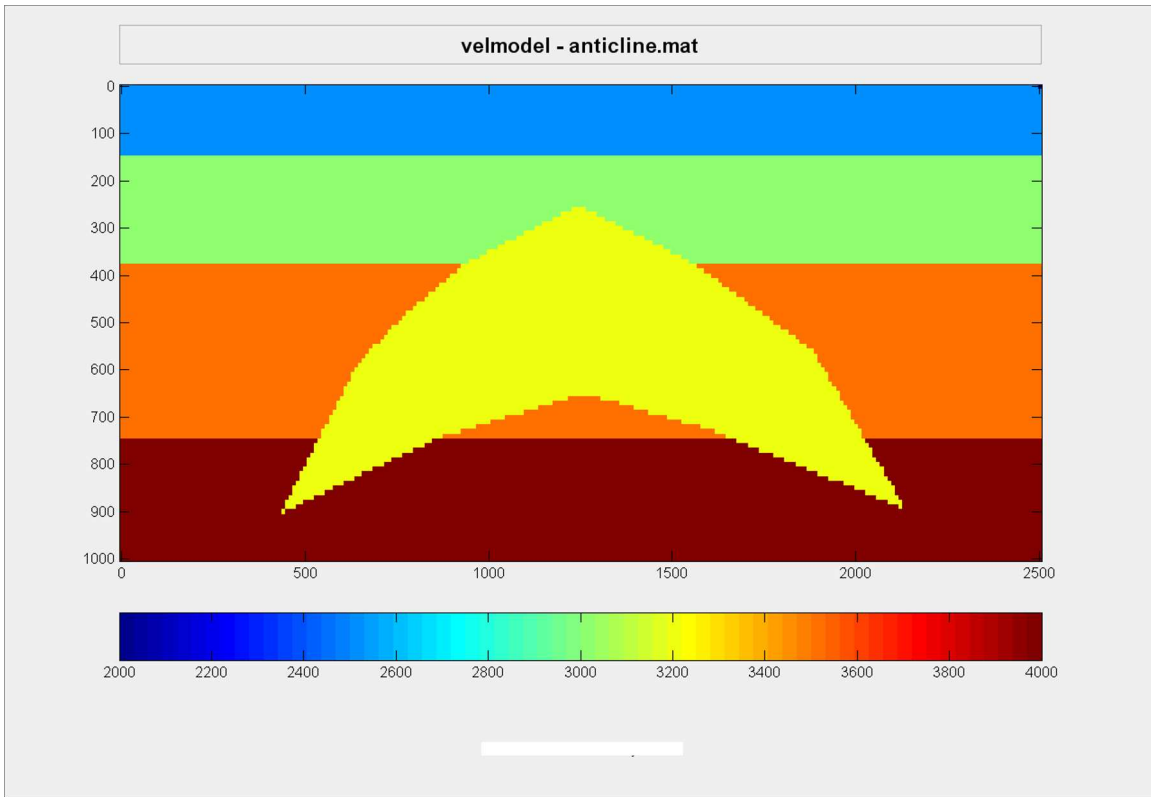
FIG. 24: Anticline embedded velocity model
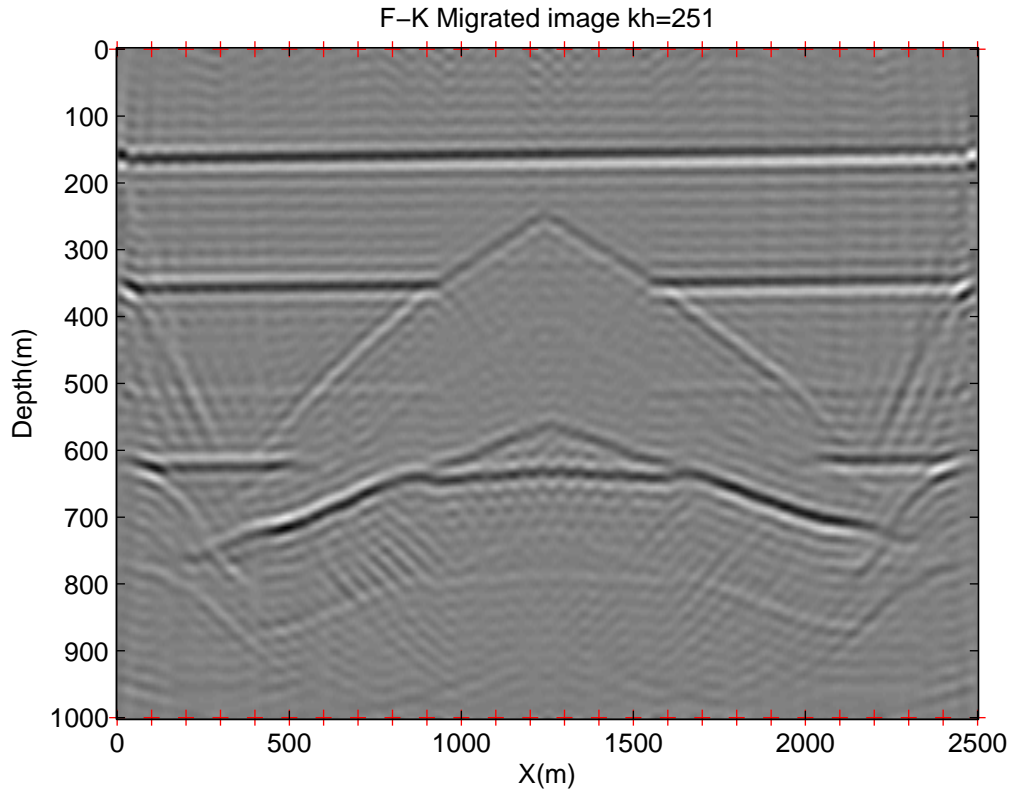
FIG. 25: Anticline embedded velocity model, deconvolved synthetic data, x=1195m
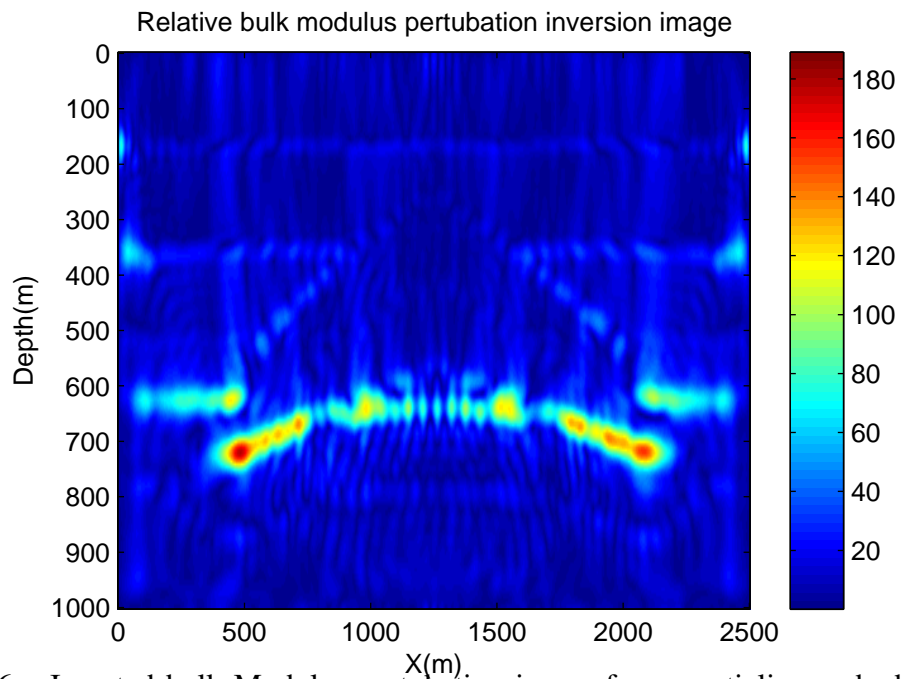
FIG. 26:   Inverted bulk Modulus pertubation image for an anticline embedded velocity model
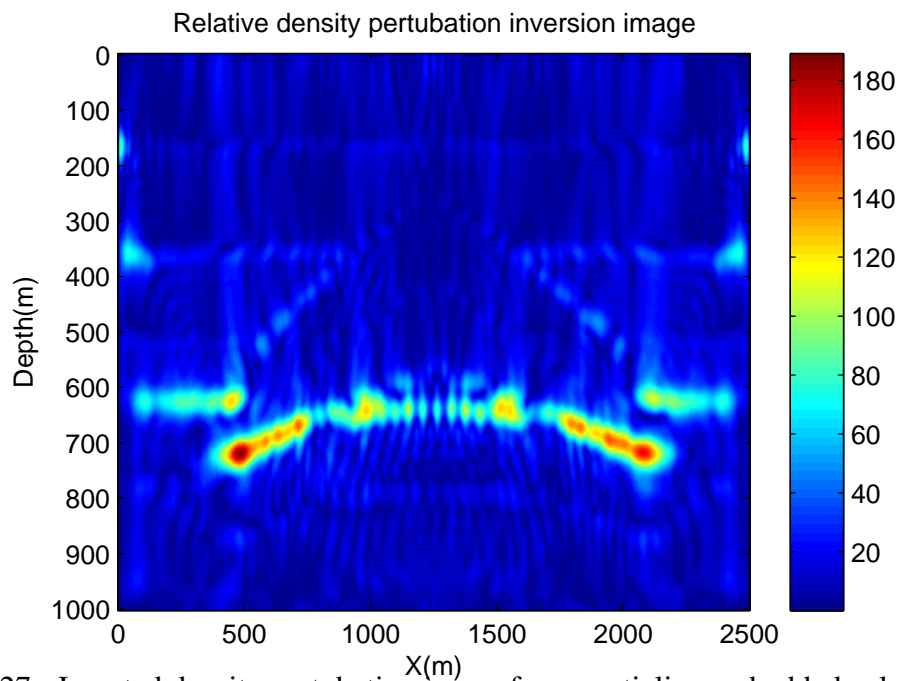
FIG. 27:   Inverted density pertubation image for an anticline embedded velocity model

Relative bulk modulus pertubation inversion image

FIG. 28:   Inverted bulk modulus pertubation image for an anticline embedded velocity model 120 half-offsets

Relative density pertubation inversion image

FIG. 29: Inverted density pertubation image for an anticline embedded velocity model for 120 half-offsets

SUMMARY AND CONCLUSION

In this project the inversion algorithm in the Fourier domain from Clayton and Stolt (1981) is implemented in MATLAB code and tested. We examine only the constant background velocity case and setup four cases to test various aspect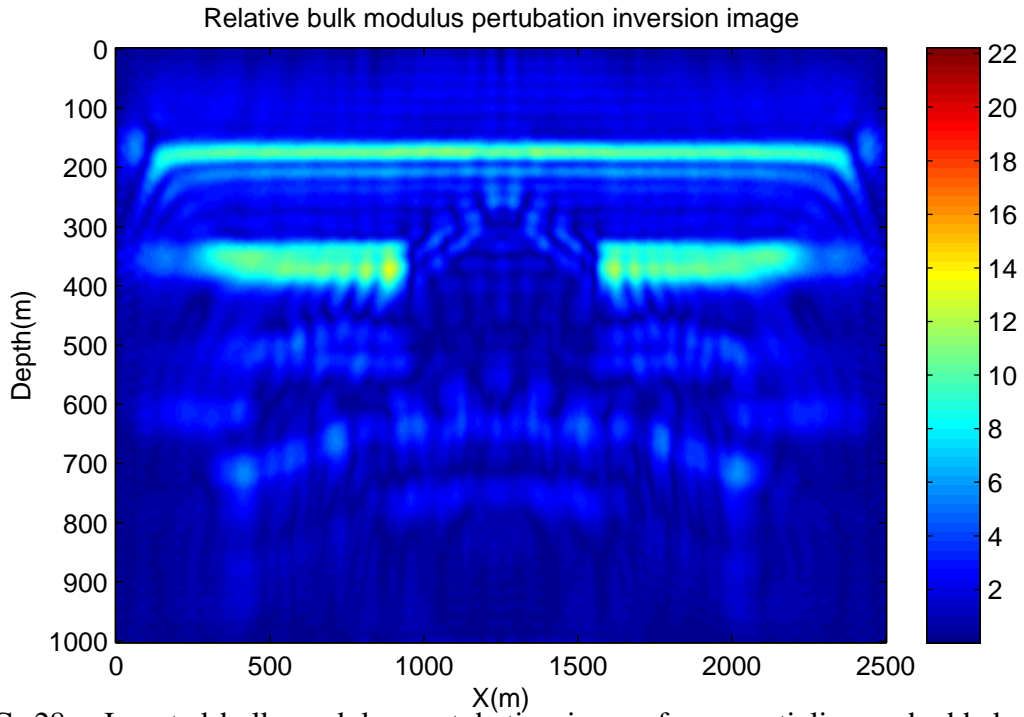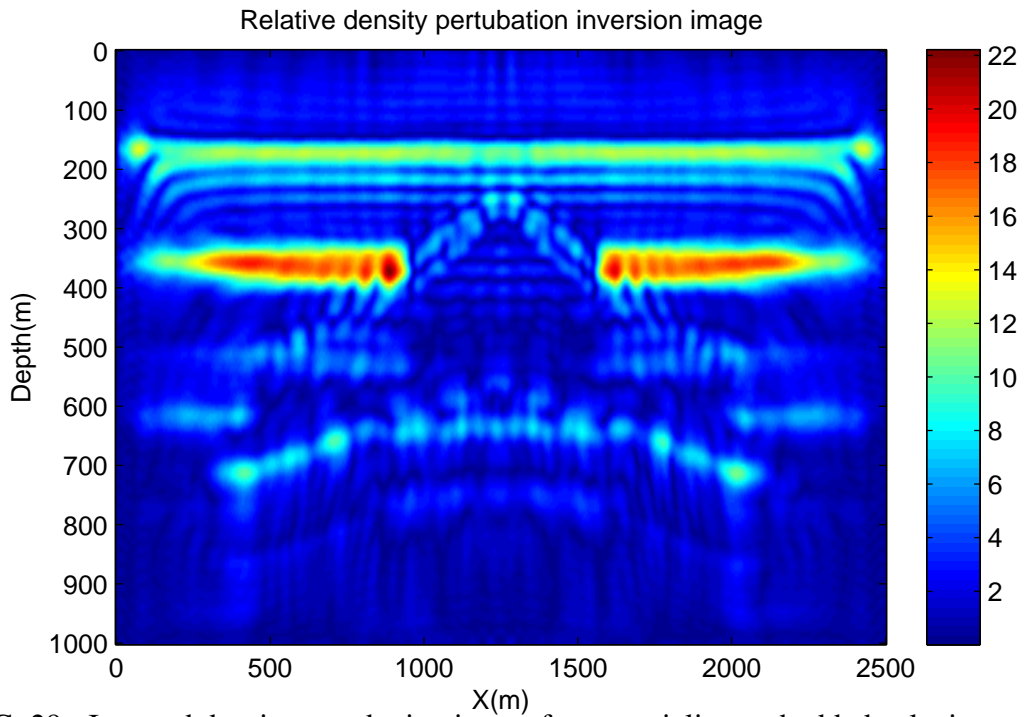s of the inversion. What can be concluded is that linearized Born inversion works for all cases, testing indicates the algorithm will produce a very good solution for the 1.5D cases with flat layer geometry.

The single layer high velocity differential produced the same structural image as that of the migrated, deconvolved input images, the inversion produced bulk modulus and density pertubation images clearly showing the location of the pertubation. The computed velocity image has the same velocity amplitudes as the velocity model including the 1500 m/s pertubation found at the interface between layers.

The four layer case was more complex but produced clear images as well, because of the least squares inversion method any noise in a given input image is smoothed out when a stack of images are summed and averaged. The bulk modulus and density pertubation images show a progresive increase in velocity differential from the background velocity, these show up as more intense boundaries and is what was expected.

For the 2-D cases the results are a little more complex but still useful to note, the shallow low velocity embedded body produced a migrated image with fairly strong ghosting artefacts. Especially in the lower layers where the contrast between the high velocity deep layers and the body is the greatest. The resulting inversion images are surprisingly clear, the multiples seen in a given migrated images have been smoothed out to a large extent.

However another issue arises where a form of 'beading' occurs along all the non horizontal boundaries in the inversion images of both 2D models. The size of these bright beads is approximately that of the grid spacing the cause of which is explained in the section on the shallow velocity model, this effect shows up in both 2-D model runs. Computing the velocity pertubation image from the K and ρ pertubation images yields a very noisy image which is generally correct in the location of the pertubation but the amplitude of the velocity changes do not match the initial velocity model.

For the final case of the anticline structure the results are generally the same as the embedded low velocity body, the difference here is that the anticline structure has an internal velocity which is higher then the first two layers but lower then the deepest two layers. This was done to test how the amplitude of the pertubation changed with both depth and with relative dip angle.

The migrated image has a lot of noise from point diffractions from the edges of the flat layers and from the sharp corners of the tips of the anticline structure. The resulting inversion and the pertubation images again show that most of this noise is smoothed out in the process. The amplitude of the pertubation increases with depth. The edges of the anticline become progressively more intense as the difference in velocity between the horizontal media and the body become relatively greater.

Other effects mentioned in the Clayton and Stolt (1981) paper were examined as well,

adding more images with larger k_h resulted in pertubation images in K and ρ with differing amplitude scales. This was most clearly seen in the anticline model where the number of k_h images used in the inversion was tripled. The amplitudes between K and ρ clearly favored a weighting towards a greater variation in density rather then bult modulus to produce variations in velocity.

A second effect shows up which is also mentioned in the paper, the k_h/k_z ratio was not maintained when calculating the inversion for a large number of offsets. This caused a the resolution of the image to change with depth, becoming shallower and emphasizing the shallower layers. The remedy for this effect is to maintain the same ratio by increasing the number of k_z values used.

The model which worked out the best in testing seems to have been the flat, multi-layered model which had moderate velocity changes between layers, while the single layer model yielded a correct velocity differential while the other models had values which fell short of the expected values.

The issues which need to be examined and resolved is the noise generated by diffraction at the ends of the interface layers. This is not accounted for in the forward modeling routine and needs to be compensated for; the next steps in refining this method are:

- Determine why the pertubation velocity falls short of the expected values for cases other then the single interface model.

- Incorporate and test an analytical source solution, in this case using the equations developed in Alford et al. (1974), the method on how to accomplish this is described in Mosco et al. (2007).

- Improve the accuracy of the Laplacian forward difference operator by going to a sixth order scheme, hence allowing even higher velocity changes(ie dynamic range) and a smaller grid size. The cost will be in terms of computational time which may change by an order of magnitude.

- Elimination and suppression of the sources of noise from the model, this is primarily directed to eliminating the point source diffraction effects coming from the sides of the model.

- More efficient computational schemes such a parallel processing need to be implemented for more complex, higher resolution datasets. Otherwise this method becomes prohibitively expensive in terms of computational resources and time required to do the migration and inversions.

APPENDIX A

Table 1: Model Run input parameter values

Model Size	2500mx1000m
Model Grid Spacing	5m
Model Time Sampling Rate	4ms
Model Time Step	0.5ms
Number Sources	500
Number Recievers	500
Number of Shotpoints	500
Receiver Spacing	5m

Table 2: Table of Velocity model parameters for 5m grid models.

Velocity Model	Reflector#	Depth(m)	Layer #	Velocity(m/s)	R Coeff
Flat single reflector	1	300	1	2500	0.2308
			2	4000	
Flat multilayer	1	310	1	2500	0.0476
	2	315	2	2750	0.0435
	3	670	3	3000	0.0400
	4	675	4	3250	0.0370
	5	980	5	3500	0.0345
	6	985	6	3750	0.0323
			7	4000	
Anticline	1	145	1	2500	0.0476
	2	150	2	2750	0.0435
	3	380	3	3000	0.0400
	4	385	4	3250	0.0370
	5	750	5	3500	0.0345
	6	755	6	3750	0.0323
			7	4000	
			body	3200	
			body_top	3100.4	
			body_bottom	3350	
Low Velocity channel	1	120	1	2500	0.0476
	2	125	2	2750	0.0435
	3	460	3	3000	0.0400
	4	465	4	3250	0.0370
	5	840	5	3500	0.0345
	6	845	6	3750	0.0323
			7	4000	
			body	2397.6	
			body_top	2698.8	
			body_bottom	2948.8	

APPENDIX B: MATHEMATICAL APPENDIX

BASIC SCATTERING THEORY

In the field of forward scattering(Clayton and Stolt (1981)) the Lippmann-Schwinger equation is crucial for solving acoustic scattering problems, the derivation of this equation can be found in [reference to L-S derivation here] this equation is given by

$$G = G_r + G_r V G, \tag{16}$$

where V is the scattering potential and G is the Green's function operator which is the solution to the linear isotropic acoustic wave equation

$$LP = \left(\frac{\omega^2}{K} + \nabla \cdot \frac{1}{\rho} \nabla \right) P = 0, \tag{17}$$

where

$$L = \left(\frac{\omega^2}{K} + \nabla \cdot \frac{1}{\rho} \nabla \right), \tag{18}$$

and L for the reference medium is

$$L_r = \left(\frac{\omega^2}{K_r} + \nabla \cdot \frac{1}{\rho_r} \nabla \right), \tag{19}$$

so the Green's function is simply the inverse of this operator.

$$G = L^{-1}, \tag{20}$$

and where ρ and K are the density and bulk modulus respectively. G and G_r are the Green's function perturbation and the Green's function reference operator (the slowly varying background about which it is perturbed).

This has is only a very brief overview of the essential basis of scattering theory, a more through examination requires a detailed understanding of Partial Differential Equation methods such as Transform methods see Constanada (2010), plus the use of Green's function operator methods see Duffy (2001). For a through mathematical approach to multidimensional inversion the book by Bleistein et al. (2001) is recommended. The application of Green's theorem to many types of problems in geophysics can be found in the review paper by Ramirez et al. (2009). A very through review of inverse scattering theory and it's application in seismic exploration can be found in Weglein et al (2003).

The Inversion Algorithm for a Constant Background

We will follow the inversion algorithm outlined in Clayton and Stolt (1981) and use their notation as well. The Born approximation of the Lippmann-Schwinger equation is given by the series expansion of the implicit equation

$$G = (I - G_r V)^{-1} G_r, \tag{21}$$

which related the Green's operator G in the actual medium and the reference operator G_r and which can be expanded as a series called the Born-Neumann series see Morse and Feshbach (1953) .

$$G = G_r \sum_{i=0}^{\infty} (VG_r)^i. \tag{22}$$

We approximate the total wavefield truncating the expansion. The direct wave in the wavefield is the zeroth order term, G_r and the primary reflections are approximated by the first order term $G_r V G$.

So for the direct wave and the primary reflections we will have

$$G = G_r + G_r V G. \tag{23}$$

Subtraction of the Direct Wave from the Gathers

The observed wavefield D is defined as $D = (G - G_r)S(\omega)$, and so

$$D = (G - G_r)S(\omega) = (G_r V G)S(\omega). \tag{24}$$

Consequently in order to do a proper inversion of the wavefield, the direct wave G_r first needs to be subtracted from the seismic profiles. This is done for the current testing purposed by directly subtracting the two wavefields G and G_r.

Deconvolution and Subtraction of the Wavelet

Before the inversion can be done the source wavelet must be subtracted or deconvolved from the transformed wavefield as illustrated below, a small stability factor ϵ has been added to the algorithm to prevent any singularities from occurring during this operation.

$$D'(k_m, k_h, k_z) = \frac{-1}{\rho_r} \frac{D(k_m, k_h, \omega)}{S(\omega) + \epsilon}, \tag{25}$$

Direct Inversion

The first step in the inversion is to Fourier transform the wavefield from source x_g and receiver x_s coordinates to source-receiver wavenumbers k_g, k_s, we will drop the prime notation of the deconvolved wavefield for convenience.

$$D(k_g, k_s, \omega) = \frac{1}{2\pi} \int \mathrm{d}x_g \int \mathrm{d}x_s e^{-ik_g x_g} D(x_g, x_s, \omega) e^{ik_s x_s}, \tag{26}$$

$$= \int \mathrm{d}x' \int \mathrm{d}z' G_r^+(k_g, 0|x', z'; \omega) V(x', z'; \omega) G_r^+(x', z'|k_s, 0|; \omega) S(\omega), \tag{27}$$

Where $G_r^+(k_g, 0|x', z'; \omega)$ and $G_r^+(x', z'|k_s, 0|; \omega)$ are Green's operators and have the form given by

$$G_r^+(k_g, 0 | x', z'; \omega) = \frac{i\rho_r}{\sqrt{2\pi}} \frac{e^{-i(k_g x' - q_g |z'|)}}{2q_g}, \tag{28}$$

$$G_r^+(x', z' | k_s, 0 |; \omega) = \frac{i\rho_r}{\sqrt{2\pi}} \frac{e^{i(k_s x' + q_s |z'|)}}{2q_s}, \tag{29}$$

and

$$q_g = \frac{\omega}{\nu_r} \sqrt{1 - \frac{\nu_r^2 k_g^2}{\omega^2}}, \tag{30}$$

$$q_s = \frac{\omega}{\nu_r} \sqrt{1 - \frac{\nu_r^2 k_s^2}{\omega^2}}, \tag{31}$$

So placing the Green's operators into the integral equation we get

$$D(k_g, k_s, \omega) = \frac{-\rho_r^2}{2\pi} \int dx' \int dz' \frac{e^{-i(k_g x' - q_g |z'|)}}{2q_g} V(x', z'; \omega) \frac{e^{i(k_s x' + q_s |z'|)}}{2q_s} S(\omega), \tag{32}$$

Here V is the scattering potential or the structure we are trying to image, this potential is given by the difference of the two wave operators L and L_r

$$V = \left(\frac{\omega^2}{K} - \frac{\omega^2}{K_r} \right) + \nabla \cdot \left(\frac{1}{\rho} - \frac{1}{\rho_r} \right) \nabla, \tag{33}$$

Replacing K and ρ by dimensionless media operators as follows

$$L = \omega^2 \frac{a_1}{K} + \nabla \cdot \frac{a_2}{\rho} \nabla, \tag{34}$$

where a_1, a_2 are

$$a_1 = \left(\frac{K_r}{K} - 1 \right), a_2 = \left(\frac{\rho_r}{\rho} - 1 \right), \tag{35}$$

Now evaluating the equation relating the data to the scattering potential using V above

$$\begin{aligned} D(k_g, k_s, \omega) = &\frac{-\rho_r^2}{2\pi} \int dx' \int dz' \frac{e^{-i(k_g x' - q_g |z'|)}}{2q_g} \left[\left(\frac{\omega^2}{K} - \frac{\omega^2}{K_r} \right) \right. \\ &+ \nabla \cdot \left(\frac{1}{\rho} - \frac{1}{\rho_r} \right) \nabla \left] \frac{e^{i(k_s x' + q_s |z'|)}}{2q_s} S(\omega), \right. \end{aligned} \tag{36}$$

and and substituting in a_1 and a_2 then integration by parts we get

$$
\begin{aligned}
D(k_g, k_s, \omega) =& \frac{-\rho_r^2}{2\pi} \int \mathrm{d}x' \int \mathrm{d}z' \frac{e^{-i[(k_g-k_s)x'-(q_g+g_s)z')]}}{4q_gq_s} \times \\
& \left[\frac{\omega^2}{\nu_r^2} a_1(x', z') + (q_gq_s - k_gk_s)a_2(x', z') \right] S(\omega),
\end{aligned}
\tag{37}
$$

Note the absolute value signs around z' are dropped if we assume $a_1(x, z)$ and $a_2(x, z)$ are zero for $z < 0$.

The above equation is of the same form as a double Fourier transform in the x' and z' variables if we do some rearranging

$$
\begin{aligned}
D(k_g, k_s, \omega) =& \frac{-\rho_r^2 S(\omega)}{2\pi 4q_gq_s} \int e^{-i(k_g-k_s)x'} \int e^{i(q_g+g_s)z'} \times \\
& \left[\frac{\omega^2}{\nu_r^2} a_1(x', z') + (q_gq_s - k_gk_s)a_2(x', z') \right] \mathrm{d}z' \, \mathrm{d}x',
\end{aligned}
\tag{38}
$$

the result of the evaluation yields

$$
\begin{aligned}
D(k_g, k_s, \omega) =& \frac{-\rho_r^2 S(\omega)}{4q_gq_s} \left[\frac{\omega^2}{\nu_r^2} a_1(k_g - k_s, -q_g - q_s) \right. \\
& \left. + (q_gq_s - k_gk_s)a_2(k_g - k_s, -q_g - q_s) \right],
\end{aligned}
\tag{39}
$$

Change of Coordinates to ω, q_g, q_s space

In order to solve for a_1 and a_2 we will need to change to midpoint/offset coordinates from the source/receiver system.

We have the following definitions the midpoint wavenumber $k_m = k_g - k_s$,
the half offset wavenumber $k_h = k_g + k_s$
which in the space domain x,z correspond to

$$
x_m = \frac{x_g + x_s}{2}
\tag{40}
$$

and

$$
x_h = \frac{x_g - x_s}{2}
\tag{41}
$$

and a new independent variable

$$
k_z = -q_g - q_s = -\frac{\omega}{\nu_r} \sqrt{1 - \frac{\nu_r^2 k_g^2}{\omega^2}} - \frac{\omega}{\nu_r} \sqrt{1 - \frac{\nu_r^2 k_s^2}{\omega^2}},
\tag{42}
$$

Solving for ω, q_g and q_s we have the expressions

$$\omega(k_m, k_h, k_z) = -\frac{\nu_r k_z}{2}\sqrt{(1 + \frac{k_m^2}{k_z^2})(1 + \frac{k_h^2}{k_z^2})}, \tag{43}$$

$$q_g(k_m, k_h, k_z) = -\frac{k_z}{2}(1 - \frac{k_m k_h}{k_z^2}), \tag{44}$$

$$q_s(k_m, k_h, k_z) = -\frac{k_z}{2}(1 + \frac{k_m k_h}{k_z^2}, \tag{45}$$

Now that we have expressions for ω, q_g, q_s the the Direct Fourier transform computed in these coordinates and data can be transformed back after the inversion.

Writing the equation for the wavefield using these new variables substituted according to the definitions above we get

$$D(k_m, k_z, k_h) = \frac{-\rho_r^2 S(\omega)}{4q_g q_s}\left[\frac{\omega^2}{\nu_r^2}a_1(k_m, k_z) + (q_g q_s - k_g k_s)a_2(k_m, k_z)\right], \tag{46}$$

When transformation variables are substituted in and simplified we obtain the system of equations which need to be inverted.

$$D(k_m, k_z, k_h) = -\rho_r\left[\sum_{i=1}^{2} A_i(k_m, k_h, k_z)a_i(k_m, k_z)\right]S(\omega), \tag{47}$$

where

$$A_1 = (k_m, k_h, k_z) = \frac{1}{4}\frac{(k_z^2 + k_h^2)(k_z^2 + k_m^2)}{k_z^4 - k_m^2 k_h^2}, \tag{48}$$

and

$$A_2 = (k_m, k_h, k_z) = \frac{1}{4}\frac{(k_z^2 - k_h^2)(k_z^2 + k_m^2)}{k_z^4 - k_m^2 k_h^2}, \tag{49}$$

so we must compute D' as follows

$$D'(k_m, k_z, k_h) = \frac{-1}{\rho_r}\left[\frac{D'(k_m, k_z, k_h)}{S(\omega)}\right], \tag{50}$$

After the deconvolution stage we are left with

$$D'(k_m, k_z, k_h) = \left[\sum_{i=1}^{2} A_i(k_m, k_h, k_z)a_i(k_m, k_z)\right], \tag{51}$$

of which we need to determine the $a_i(k_m, k_z)$ through perhaps a least squares method.

APPENDIX C: AN IRREGULAR HIGH VELOCITY BODY

This model is included as an appendix in this paper as a test of both the migration/inversion algorithm and because it does not add significantly to the main discussion but helps to further illustrate points made in the main text.

The velocity model (fig.30) is of a body of irregular shape and size, the background velocity is the same as previous models at 2500 m/s. The velocity of the body is set to 6000 m/s, geologically this model might be seen with a shallow subsurface volcanic intrusion with the magma chamber filled with solidified felsic(granitic) material, ie a pluton. The most noticeable features here is the body itself is completly surrounded in low velocity material, there are no other layers present to reflect seismic energy back into the body from below.

The migrated image in figure 31 displays clearly the upper surface in the correct orientation and depth, the curvilinear nature is also imaged correctly. The areas which are not imaged and have no reflections are the steeply dipping portions of the rounded body on the left side and the vertical feature on the right. Imaging the reflector on the bottom side of this body is much more challenging, the relatively linear, sloped section is not in the correct position though the depth and dip are approximately correct.

The images of the pertubations in bulk modulus (fig.32) and density (fig.33) reproduce the migrated images, with the exception that internal body features are for the most part averaged out during the inversion stage. As in the anticline case, a large number of k_h values were used, 150 in this case but also the corresponding number of k_z values were increased to 75 from 50. This avoided the selective resolution effect mentioned in the Clayton and Stolt (1981) paper.

The relative amplitudes of the two pertubation images are also distinctly different, with the density pertubatiobn being much stronger then the bulk modulus. There is a large bright red feature which shows up in the density pertubation image at x=1400m, this hotspot is due to a tuning effect of seismic waves. In the original velocity model at this position is a narrowing on the body so that the lower and upper reflectors come within about 50m of each other, the two reflectors are interfering with each other reinforcing the amplitude of the feature at that position.

In figure 34 we can see some features in this noisy image which do follow what is expected from the model. The upper surface reflector has a relatively large negative velocity change, the lower sloped reflector, although in the wrong position shows a large positive velocity change. This is what is expected when transitioning between the two media. Although there are erroneous areas such as the more steeply dipping portions of the upper reflector which shows the opposite velocity from the rest of the reflector, this is because combining the bulk modulus and density pertubation maps there are areas of almost zero pertubation in the bulk modulus image which causes a sign change when computed using equation 10.
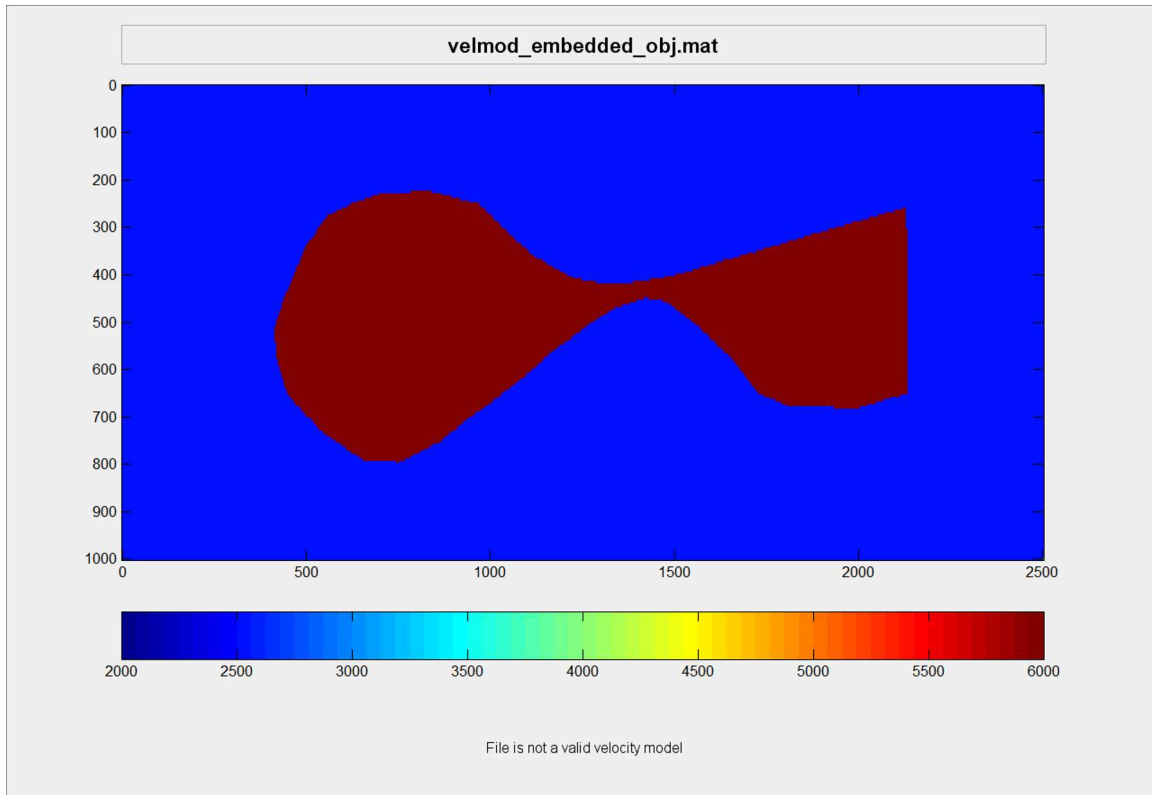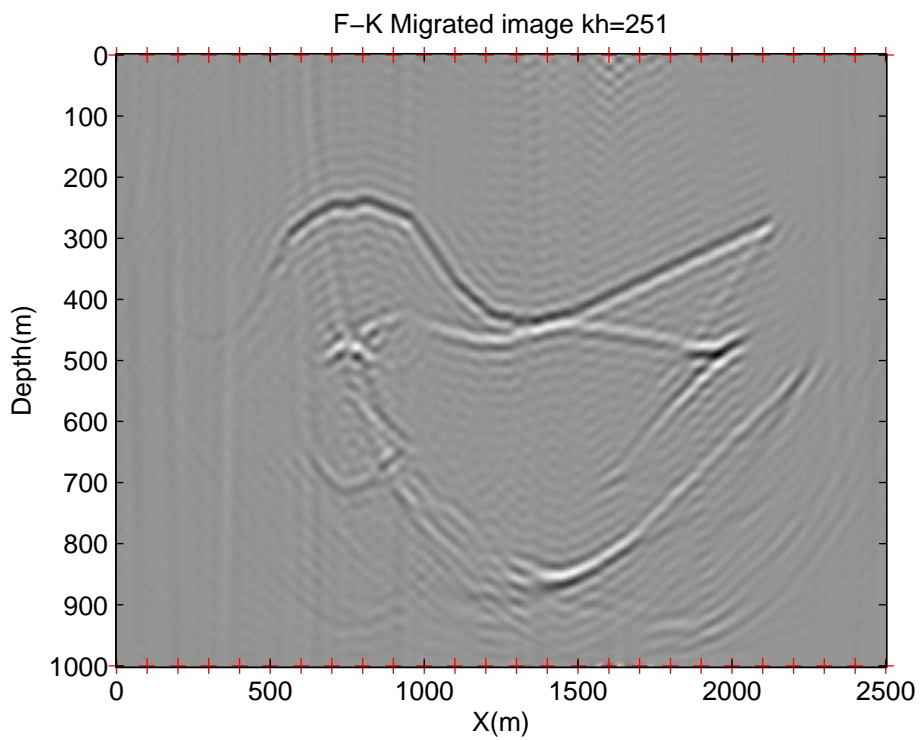
FIG. 30: Irregular high velocity model

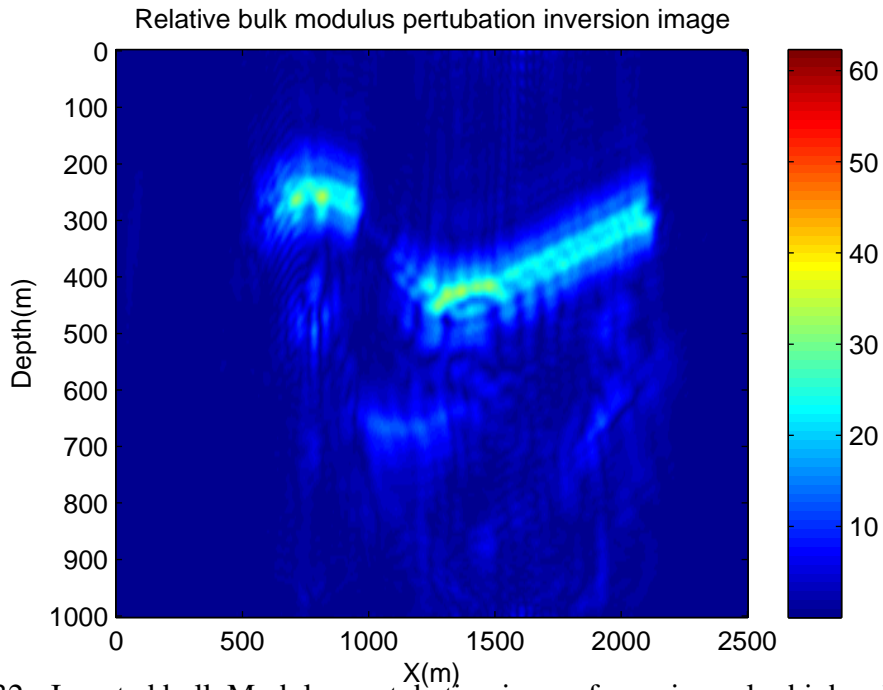FIG. 31: Irregular high velocity model, deconvolved synthetic data, x=1195m

Relative bulk modulus pertubation inversion image

FIG. 32: Inverted bulk Modulus pertubation image for an irregular high velocity model
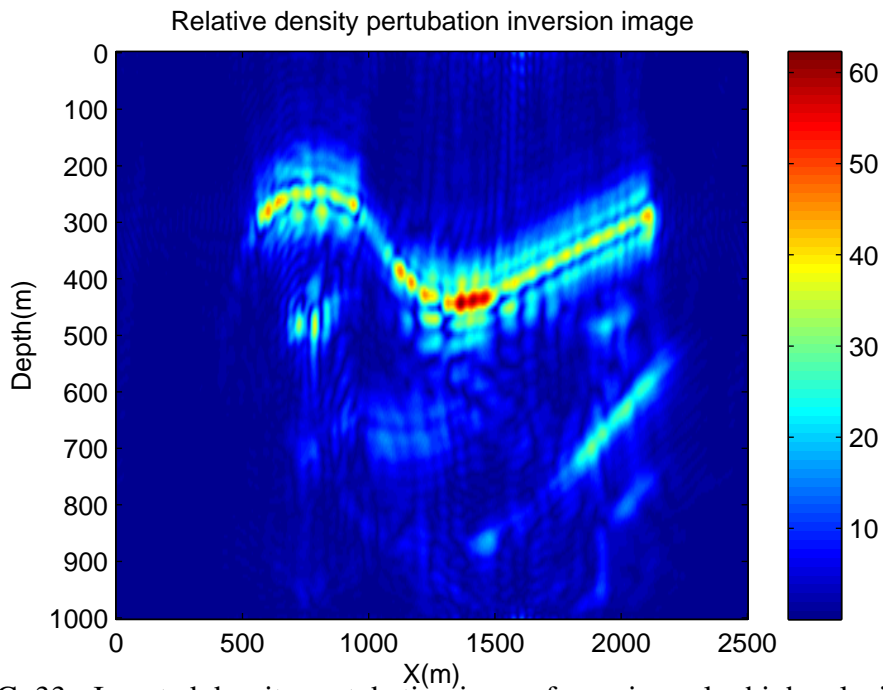
Relative density pertubation inversion image

FIG. 33: Inverted density pertubation image for an irregular high velocity model
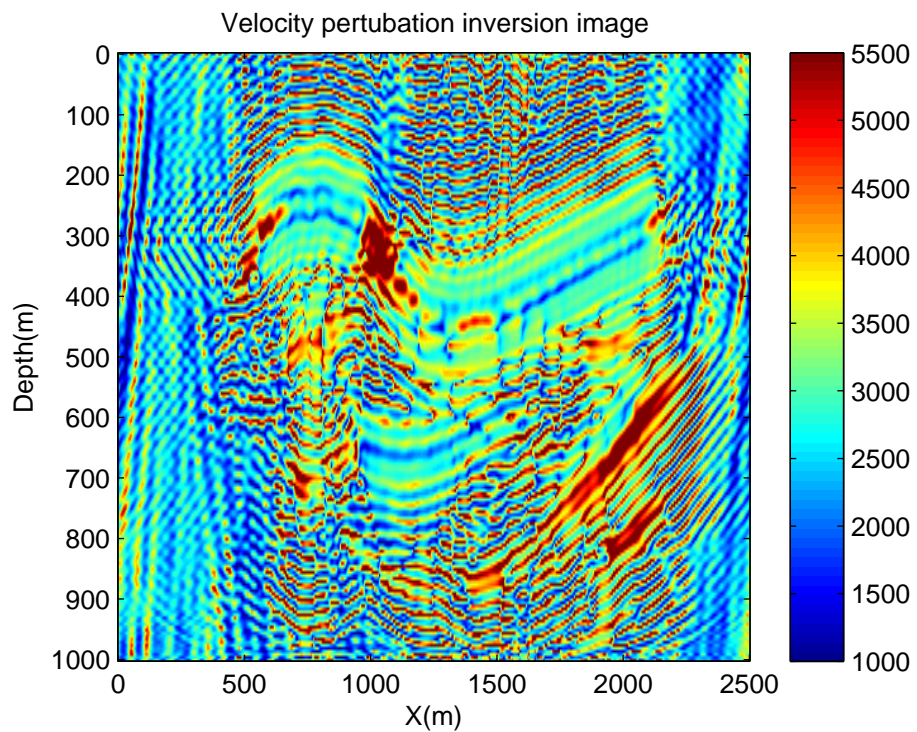
FIG. 34: Velocity pertubation image for the irregular high velocity model

REFERENCES

Alford, R.M., K.R. Kelly, and D.M.Boore, 1974, Accuracy of Finite-difference modeling of the acoustic wave equation ,Geophysics, 39, 834-842.

Aki, K., and P. G. Richards, 2002, Quantitative Seismology (2nd ed.): University Science Books

Bleistein, N., J. Cohen and J. Stockwell, 2001, Mathematics of Multidimensional Seismic Imaging, Migration and Inversion: Springer-Verlag.

Bording, Ralph P., and Larry Lines, 1997, Seismic Modeling and Imaging with the Complete Wave Equation, SEG Course Notes No.8, Society of Exploration Geophysicists

Claerbout, J. F., 1968, Synthesis of a layered medium from its acoustic transmission response: Geophysics, 33, 264-269.

Clayton, A.W. and Stolt, R.H, 1981, A Born-WKBJ inversion method for acoustic reflection data, Geophysics, 46, 1559-1567.

Constanada, C., 2010, Solution Techniques for Elementary Partial Differential Equations: Chapman and Hall/CRC

Duffy, D.G., 2001, Green's Functions with Applications: Chapman and Hall/CRC

Garcia D, Robust smoothing of gridded data in one and higher dimensions with missing values., 2010, Computational Statistics and Data Analysis, 54, 1167-1178. Elsevier

Innanen, K., 2010, A theoretical note on scattering and diffraction of radar waves from a seismic disturbance propagating in the near-surface, CREWES Research Reports, 22

Morse, P., and H. Feshbach, 1953, Methods of Theoretical Physics, Part 1. McGraw-Hill.

Moczo, P., Robertsson, J.O.A., and Eisner, L., 2007, The Finite Difference Time-Domain Method for Modeling of Seismic Wave Propagation, Advances in Geophysics, 48, 421-516, Elsevier-Academic Press.

Ramirez, A.C., and A. Weiglein, 2009, Green's theorem as a comprehensive framework for data reconstruction, regularization, wavefield separation, seismic interferometry, and wavelet estimation: A tutorial: Geophysics, 74, W35-W62

van Trier, J., 1986, Inversion of seismic data in the Fourier domain and prestack Stolt migration, Stanford Exploration Project Report, 48, 227-241

Arthur B Weglein, Fernanda V Araújo, Paulo M Carvalho, Robert H Stolt, Kenneth H Matson, Richard T Coates, Dennis Corrigan, Douglas J Foster, Simon A Shaw1, and Haiyan Zhang, 2003, Inverse scattering series and seismic exploration, Inverse Problems, 19, R27-R83

Yilmaz, O., 2001, Seismic Data Analysis: Processing, Inversion and Interpretation of Seismic Data, 2nd edition: SEG Publishing

Young, G.R., Kris Innanen and Laurence R Lines, 2011, Multiparameter inverse scattering: computational approaches, CREWES Research Report 2011, 23